

VESSEL TRACTOGRAPHY USING AN INTENSITY BASED TENSOR
MODEL

by
Süheyla Çetin

Submitted to the Graduate School of Engineering and Natural Sciences
in partial fulfillment of
the requirements for the degree of
Master of Science

Sabancı University
Spring 2010-2011

VESSEL TRACTOGRAPHY USING AN INTENSITY BASED TENSOR MODEL

APPROVED BY

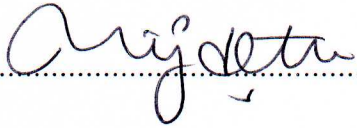
Assist. Prof. Dr. Gzde NAL
(Thesis Supervisor)



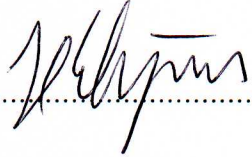
Assoc. Prof. Dr. Mustafa NEL



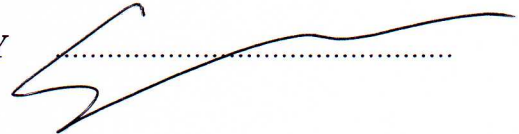
Assist. Prof. Dr. Mjdat ETİN



Assist. Prof. Dr. Hakan ERDOĖAN



Assist. Prof. Dr. Selim BALCISOY



DATE OF APPROVAL:

©Süheyla Çetin 2011

All Rights Reserved

to my family

Acknowledgments

I wish to express my gratitude to my supervisor, Gözde Ünal, whose expertise, understanding, and patience, added considerably to my graduate experience. I am grateful to her not only for the completion of this thesis, but also for her unconditional support from the beginning.

I would like to thank to our clinical partner Yeditepe Cardiology Department, especially cardiologist Prof. Dr. Muzaffer Değertekin for his valuable guidance and support.

I also would like to thank TÜBİTAK for providing the necessary financial support for my graduate education¹.

I am grateful to my committee members Mustafa Ünel, Müjdat Çetin, Hakan Erdoğan, and Selim Balcısoy for taking the time to read and comment on my thesis.

I owe special thanks to all my friends and colleagues, particularly to, Demet Yılmaz, Ali Demir, Mehmet Umut Şen, Gözde Gül Işgüder and Andaç Hamamcı for their friendship and assistance.

Finally, I would like to thank my family Mesut, Hülya, Saadet, Sena and Ukbe for their valuable supports, love and belief in me.

¹This work was supported by Tübitak Grant No:108E126”Medical Image Analysis for Monitoring of Cancer Disease using Brain Magnetic Resonance ImagingGrant” and Grant No:108E162:”Assessment of Fluid Tissue Interaction Using Multi-Modal Image Fusion for Characterization and Progression of Coronary Atherosclerosis”.

VESSEL TRACTOGRAPHY USING AN INTENSITY BASED TENSOR MODEL

Süheyla Çetin.

EE, M.Sc. Thesis, 2011

Thesis Supervisor: Gözde ÜNAL

Keywords: segmentation, CTA, tubular structures, branch detection, vessel trees, coronary arteries, tensor estimation, tractography, tensor

Abstract

In the last decade, CAD (Coronary Artery Disease) has been the leading cause of death worldwide [1]. Extraction of arteries is a crucial step for accurate visualization, quantification, and tracking of pathologies. However, coronary artery segmentation is one of the most challenging problems in medical image analysis, since arteries are complex tubular structures with bifurcations, and have possible pathologies. Moreover, appearance of blood vessels and their geometry can be perturbed by stents, calcifications and pathologies such as stenosis. Besides, noise, contrast and resolution artifacts can make the problem more challenging. In this thesis, we present a novel tubular structure segmentation method based on an intensity-based tensor that fits to a vessel, which is inspired from diffusion tensor image (DTI) modeling. The anisotropic tensor inside the vessel drives the segmentation analogously to a tractography approach in DTI. Our model is initialized with a single seed point and it is capable of capturing whole vessel tree by an automatic branch detection algorithm. The centerline of the vessel as well as its thickness is extracted. We demonstrate the performance of our algorithm on 3 complex tubular structured synthetic datasets, and on 8 CTA (Computed Tomography Angiography) datasets (from Rotterdam Coronary Artery Algorithm Evaluation Framework) for quantitative validation. Additionally, extracted arteries from 10 CTA volumes are qualitatively evaluated by a cardiologist

expert's visual scores.

İMGE YEĞİNLİĞİNE DAYALI TENSÖR MODELİ KULLANAN DAMAR TRAKTOGRAFI YÖNTEMİ

Süheyla Çetin.

EE, Yüksek Lisans Tezi, 2011

Tez Danışmanı: Gözde ÜNAL

Anahtar Kelimeler: bölütleme, BTA, borumsu yapılar, dallanma algılama, damar ağaçları, koroner arterler, tensör tahmini, traktografi, tensör

Özet

Son on yılda, KAH (Koroner Arter Hastalığı) dünya çapında önde gelen ölüm nedenlerinden biri olmuştur [1]. Patolojilerin doğru görselleştirilmesi, ölçme ve izleme için arterlerin çıkarımı çok önemli bir adımdır. Ancak, arterler karmaşık dallı borumsu yapıya sahip olduklarından ve olası patolojiler taşıyabileceklerinden koroner arter bölütlemesi tıbbi görüntü analizinde en zorlu sorunlardan biridir. Bunun yanında, stentler, kalsifikasyonlar ve stenoz gibi patolojiler kan damarlarının görünümünü ve geometrisini bozabilirler. Ayrıca, gürültü, kontrast ve çözünürlük yapay olguları sorunu daha zorlu yapabilirler. Bu tezde, Difüzyon Tensör Görüntüleme (DTG) modellerinden ilham alan, damara uygun, imge yeğİnliğİne dayanan yeni bir borumsu yapı bölütleme yöntemi sunulmaktadır. Damar içerisindeki yönbağımlı tensör, bölütlemeyi, DTG içerisindeki bir traktografi yaklaşımına benzer kılmaktadır. Modelimiz tek bir tohum noktasıyla başlatılır, ve otomatik dallanma algılama algoritmasıyla tüm damar ağacını yakalama yeteğine sahiptir. Damarın merkez çizgisinin yanısıra kalınlığı da bulunur. Niceliksel sağlama için algoritmamızın performansını 3 karmaşık borumsu yapıdaki sentetik datada, ve 8 BTA (Bilgisayarlı Tomografi Anjiyografi) datasetinde gösterdik. Bunun yanısıra, 10 BTA hacminden çıkarılan arterler kardioloji uzmanı tarafından niteliksel olarak verilen görsel skorlarla değerlendirildi.

Table of Contents

Acknowledgments	vi
Abstract	vii
Özet	ix
1 Introduction	1
1.1 Medical Motivation	1
1.1.1 Anatomy of Heart	2
1.1.2 Coronary Artery Disease	3
1.1.3 Coronary Artery Imaging	3
1.2 Contributions	7
1.3 Thesis Outline	8
2 Background on Vasculature Segmentation and DTI	9
2.1 A Brief Review on Vasculature Segmentation Algorithms	9
2.1.1 Filtering	10
2.1.2 Vasculature Segmentation Algorithms	15
2.1.3 User Interaction	22
2.1.4 Branch Detection	23
2.2 DTI (Diffusion Tensor Imaging)	23
2.2.1 Magnetic Resonance Imaging (MRI)	23
2.2.2 Diffusion Tensor Imaging (DTI) basics	26
2.3 Summary	30
3 Vessel Tractography using an Intensity Based Tensor Model	31
3.1 Image preprocessing	32
3.2 Intensity Based Tensor Fitting	33
3.2.1 Vessel Lumen Thickness Estimation:	36
3.3 Vessel tractography	38
3.3.1 Centralization	42
3.4 Branch Detection - Unsupervised Clustering	44

4	Experimental Results	48
4.1	Quantitative Validation	49
4.2	Qualitative Validation	53
5	Conclusions and Future Work	65
	Bibliography	67

List of Figures

1.1	Illustration of the heart and coronary arteries, source: <i>Coronary Anatomy and Blood Flow</i> , Richard E. Klabunde.	2
1.2	Illustration of normal artery with normal blood flow (left) and an artery with plaque buildup (right), source: <i>Atherosclerosis</i> , Heathwise, Incorporated.	3
1.3	Illustrations of Left: catheter angiography, source: <i>Catheter angiography</i> , Heathwise, Incorporated (2008); Right: coronary angiograms of whole coronary tree, source: <i>Coronary Angiography</i> , Swanson Gately.	4
1.4	A coronary artery cross-section from OCT (C) and IVUS (D) images [2]. Arrows indicate the calcified plaque regions inside the vessel.	5
1.5	Visualization of the blood vessels inside the brain using MRA, source: <i>MR Images Produced at MARIARC</i> , Liverpool University, UK.	6
1.6	Top: Anatomical planes (axial, sagittal and coronal) [3] are shown inside the brain. Bottom: Cardiac CTA images. Arrows indicate LCA in (a) axial view; (b) sagittal view; (c) coronal view.	7
2.1	A comparison between the VED and Frangi’s vesselness filter. The original data is shown in the left figure, the result of VED in the middle figure and the result of Frangi’s vesselness filtering in the right figure. Arrows indicate points of interests [4].	14
2.2	A tubular surface is represented as the envelope of a family of spheres with continuously changing center points and radii [5].	18
2.3	Level set segmentation [6]. (a) Initial contour; (b) after 150 iterations; (c) after 600 iterations; (d) after 1600 iterations.	20

2.4	Segmentation of coronary arteries from CTA data [7]. Left: Initial - deformable model based only on image intensities, the artery leaks into aorta; Middle: Deformable model based on image intensities and shape prior (after 400 iterations - artery is disconnecting from aorta); Right: Deformable model based on image intensities and shape prior (after 800 iterations - the artery totally disconnected from aorta).	21
2.5	Intensity plots of orthogonal 2-D slices; Left: a thin vessel in the pelvis, Center: the artery iliaca communis, and Right: the aorta; Top: 2D cross-section from MR images, Middle: Intensity profile of slices, Bottom: 2-D sections of generated 3-D images using the new cylindrical intensity model [8].	22
2.6	Superellipsoid models with varying parameter ϵ_1 [9]. Left: $\epsilon_1 = 1.0$; Middle: $\epsilon_1 = 0.75$; Right: $\epsilon_1 = 0.25$	23
2.7	Magnetic moment of a proton, source: " <i>Basic Physics of Nuclear Medicine/ MRI & Nuclear Medicine</i> ", wikibooks.	24
2.8	Precession [10].	25
2.9	Illustration of magnetic moment applied; Left: before; Right: after.	25
2.10	Diffusion weighted Spin Echo Pulse Sequence.	26
2.11	The human body can be divided into 3 major planes: coronal dividing the body into anterior and posterior parts, transverse (axial) dividing the body into superior and inferior parts, and sagittal dividing the body into right and left parts. These planes can be moved to any position in the body and are typically used for the tomographic imaging techniques, such as MRI and CT, source: <i>Anatomy tutorial</i> , University of Minnesota.	28
2.12	Left: B_0 (DTI without gradient); Middle: FA image; Right: Color-FA image.	29
3.1	Flowchart of the vessel tractography algorithm.	33
3.2	Illustrations of the measurement model, cylinder model, and orientations on unit sphere.	34
3.3	Example of vessel lumen thickness estimation.	37

3.4	Estimated tensors for $60 \times 60 \times 60$ synthetic vessel volume.	39
3.5	Left: Color-FA map of the estimated tensors (radius 3) for the $60 \times 60 \times 60$ synthetic vessel volume; Right: Color Hue, Red: Left-Right, Green: Anterior-Posterior, Blue: Superior-Inferior direction.	40
3.6	Illustration of the vessel tractography: Centerline of the vessel (black) is shown by gray. Extracted vessel tract until the current coordinate $\mathbf{c}(u_{n-1})$ is depicted by (navy blue). On the distal part of the tract (turquoise); minor vector of the planar tensor, \mathbf{v}_3 , current location, $\mathbf{c}(u_{n-1})$, and how the tract is obtained by adding the \mathbf{v}_3 direction to the current location $\mathbf{c}(u_{n-1})$ are shown.	41
3.7	Illustration of the regions (spheres) Ω_1 and Ω_2	42
3.8	Illustration of the regions (spheres) Ω_2 and Ω_3	43
3.9	Illustration of branch detection algorithm, where the tractography direction is shown by black arrow, the estimated path until the current coordinate is depicted by green, $\frac{5}{3}\pi$ sphere cut with radius $2r$ centered at $c(u_{n-1})$ is illustrated by orange, the coordinate that first detects one or more branches is shown by a blue sphere, and referred to as c_{first} . In addition, $2r$ voxel distance for stacking of detected branches from c_{first} is shown in the sketch.	47
4.1	Extracted vessel tree from the $101 \times 101 \times 101$ synthetic vascular dataset1.	55
4.2	Extracted vessel tree from the $101 \times 101 \times 101$ synthetic vascular dataset2.	56
4.3	Extracted vessel tree from the $101 \times 101 \times 101$ synthetic vascular dataset3.	57
4.4	Illustration of different quantities for the analysis of vessel segmentation, adopted from [11]. The reference standard is illustrated as the horizontal line in the middle with annotated radius depicted as the grey region. The metrics used to evaluate the segmented coronary path are labelled above and below the reference standard. For further details on the metrics, see [11]	58
4.5	Visualization of the result from experiments for quantitative validation using the Rotterdam cardiac data set # 1.	59

4.6	Visualization of results from experiments for quantitative validation using the Rotterdam cardiac data set # 2.	60
4.7	Visualization of results from experiments for quantitative validation using the Rotterdam cardiac data set # 6.	61
4.8	Visualization of extracted arteries from CTA volumes of patient # 1 to 6. .	63
4.9	Visualization of extracted arteries from CTA volumes of patient # 7 to 10.	64
5.1	Sample sketches for the junction problem. Edges of the vessels are shown with green color. Black circle depicts the junction coordinate. Red ellipsoid indicates the single tensor fitting at the junction coordinate, where single tensor is insufficient for the representation of the junction. Purple ellipsoids illustrates the result of multiple-tensor fitting.	66

List of Tables

2.1	List of possible patterns in 2D and 3D, depending on the value of the eigenvalue. H: high, L: low, +/- indicate the sign of the eigenvalue [12]. . .	12
4.1	Segmentation results of our method on synthetic vascular images	50
4.2	Average overlap per dataset	53
4.3	Average accuracy per dataset	54
4.4	Summary	54
4.5	Comparison of top 8 methods with our method, VET, participated in Rotterdam challenge	58
4.6	Visual scores of our method on 10 CTA datasets from Pt 1 to Pt 10	62

Chapter 1

Introduction

”So the heart is the beginning of life, the Sun of the Microcosm, even as the Sun deserves to be called the heart of the world; for it is the heart by whose virtue and pulsation the blood is moved, perfected, made apt to nourish, and is preserved from corruption and coagulation; it is the household divinity which, discharging its function, nourishes, cherishes, quickens the whole body, and is indeed the foundation of life, the source of all action.”

—*William Harvey, 1628*

1.1 Medical Motivation

It is widely accepted that coronary heart disease is the leading cause of death worldwide. According to the statistics of WHO in 2004 [1], coronary heart diseases (CHD) kill approximately 7.2 million people, which accounts for 12.2% of all deaths worldwide. The most common cause for CHD, coronary artery disease (CAD), is typically caused by excessive accumulation of plaques and fats within arteries, which restrict blood flow inside the heart.

Recently, advanced imaging techniques improve the early detection, diagnosis and treatment of coronary heart diseases. Often, experts having high quality visualization systems are less probable to make wrong diagnosis. Additionally, visual models of the arteries are used in presurgical and interventional medical navigation systems for diagnosis of disease, and for better treatment options.

1.1.1 Anatomy of Heart

The heart [13] is a vital organ, which beats, each day, 100,000 times in average, pumping about 2,000 gallons (7,571 liters) of blood to the human body. Heart has 4 chambers. The upper chambers are called the left and right atria, and the lower chambers are called the left and right ventricles. The blood is forced to be pushed from left ventricle through the aortic valve and into human body. To feed myocardium (heart muscle) with oxygen and nutrients, approximately 5% of the blood is supplied from coronary arteries to the heart muscle, which is responsible for the pumping functionality of the heart and can vary from person to person. The coronary arteries consist of two main arteries, which originate from the coronary ostium (root of aorta): the right (RCA) and left coronary arteries (LCA). The left coronary artery (LM - left main) system bifurcates into the circumflex artery (LCX) and the left anterior descending artery (LAD). Left coronary artery supplies blood for left ventricle and right coronary artery feeds right ventricle. Figure 1.1 depicts four chambers (Left and Right Atria; Left and Right Ventricles) and coronary arteries (RCA, LAD (LM), LCX, LAD) of the heart. Arteries (blood vessels) surrounding the heart are shown by red.

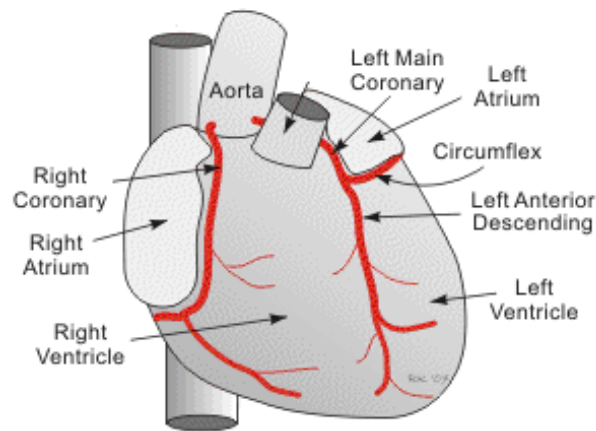


Figure 1.1: Illustration of the heart and coronary arteries, source: *Coronary Anatomy and Blood Flow*, Richard E. Klabunde.

1.1.2 Coronary Artery Disease

It is clear that CHD is a fatal disease. As the most common cause of CHD, coronary artery disease (CAD) typically begins when the inner walls of the coronary arteries are damaged because of multiple risk factors such as high cholesterol, high blood pressure, diabetes and smoking. Plaque (see Figure 1.2), which consists of cholesterol, calcium, and other substances in the blood, accumulates excessively on the damaged inner walls of the coronary arteries, which causes atherosclerosis, or hardening of the arteries [14]. Over a period of time, plaque begins to completely block the oxygen and nutrient-rich blood flow to the heart, which causes heart muscle cells to die and myocardial infarction or heart attack at the end.

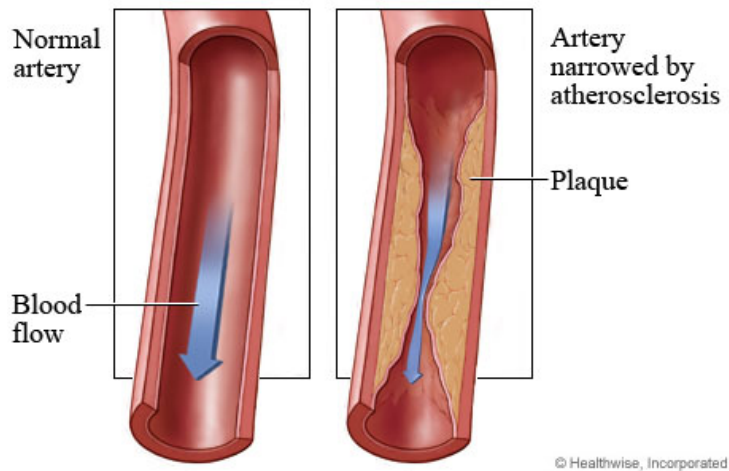


Figure 1.2: Illustration of normal artery with normal blood flow (left) and an artery with plaque buildup (right), source: *Atherosclerosis*, Heathwise, Incorporated.

1.1.3 Coronary Artery Imaging

Angiography is a minimally invasive medical test, which is a way of visualizing blood vessels. Angiography uses one of three imaging technologies and, in some cases, a radio-opaque contrast agent is injected (iodinated dyes) to highlight major blood vessels in the images. Angiography is performed using invasive and non-invasive techniques. Invasive techniques [15]: (i) X-rays with catheters; (ii) Intravascular Ultrasound (IVUS), and

Optical Coherence Tomography (OCT) and non-invasive techniques [16]: (i) Magnetic Resonance Imaging (MRI); (ii) Computed Tomography (CT) are the imaging techniques that can be used to visualize coronary arteries.

1.1.3.1 Invasive Imaging Modalities

Invasive techniques [15] include X-ray angiography, IVUS and OCT, which use catheters (a thin plastic tube) with contrast agents and imaging sensors in order to access the desired location inside the blood vessels. X-ray angiography (catheter angiography) (see Figure 1.3) has been used as a gold standard for diagnosis of coronary lesions for many years. It provides an image of arteries with high resolution. X-ray angiography [15] is performed by inserting a catheter, which is usually inserted into the groins or forearm. Once the catheter is advanced to one of the main coronary arteries, a contrast agent is injected through the tube and images are acquired using sufficient dose of ionizing radiation (x-rays). In X-ray angiography, the contrast agent is mostly needed in large doses, which can cause allergic reactions in human body. There are more drawbacks as the operation may take several hours. Furthermore, although the vessels are three-dimensional (3D), the acquired image is only two-dimensional (2D) projection of the vessels.

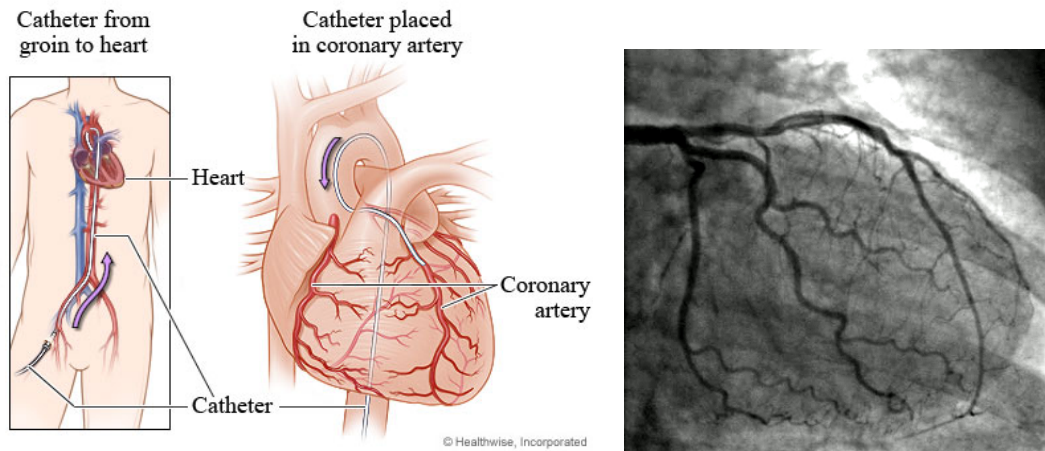


Figure 1.3: Illustrations of Left: catheter angiography, source: *Catheter angiography*, Healthwise, Incorporated (2008); Right: coronary angiograms of whole coronary tree, source: *Coronary Angiography*, Swanson Gately.

Despite limitations of X-ray angiography, it is commonly used as a guiding tool during vascular interventions. However, for high resolution plaque imaging catheter-based IVUS and OCT techniques [2](see Figure 1.4) are utilized in arterial vascular imaging, which allow real-time cross-sectional view of the lumen (interior of artery), the vessel wall and the atherosclerotic plaques. OCT and IVUS are similar as they both use a catheter, which has an imaging sensor on the tip of the catheter and advance to the desired location to acquire images. The main difference comes from collecting signals; as IVUS collects signals from reflected ultrasound beams and OCT collects signals from reflected infrared beams. OCT and IVUS technologies currently provide detailed plaque content imaging, however through a 2D cross-sectional view of the arteries.

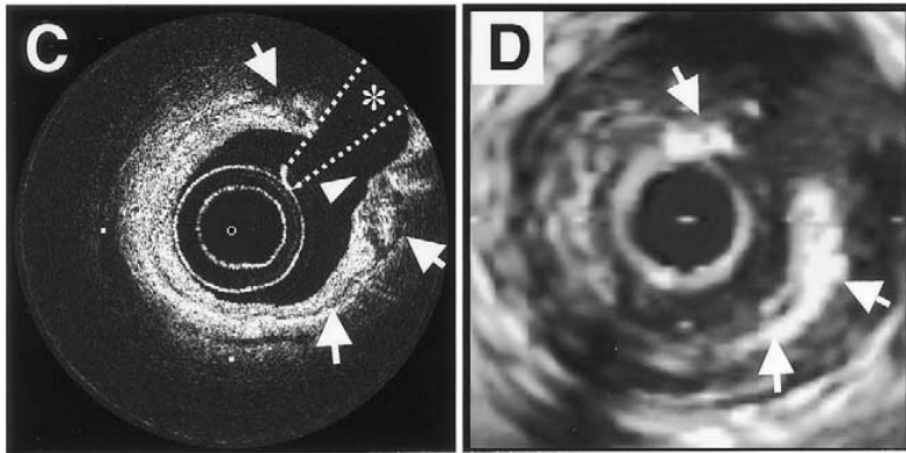


Figure 1.4: A coronary artery cross-section from OCT (C) and IVUS (D) images [2]. Arrows indicate the calcified plaque regions inside the vessel.

1.1.3.2 Non-invasive Imaging Modalities

Due to the limitations and drawbacks of invasive techniques, non-invasive imaging techniques [16] have also become popular recently. CTA and MRA are the widely used non-invasive modalities at present, which provide 3D volume imaging as compared to acquired 2D projection of vessels in X-ray angiography, IVUS and OCT.

Magnetic Resonance Angiography (MRA) [16] is an imaging technique, which is based on MRI (Magnetic Resonance Imaging), used for blood vessels visualization, especially

the motionless arteries of the neck, brain (Figure 1.5), and the legs in order to detect stenosis (abnormal narrowing), aneurysms (vessel wall dilatations) on the arteries. MRA has several drawbacks as: i) it is less successful in coronary arteries visualization, since the heart has cardiac motion; ii) it is more costly compared to other techniques; iii) it has lower resolution; and iv) it has longer scan times. However, there are several advantages of MRA over invasive catheter angiography; i) MRA is non-invasive (no need for catheter), ii) it is safer, since patient is not exposed to any ionizing radiation, and iii) Contrast agent used for MRI is less toxic than those used for invasive angiography.



Figure 1.5: Visualization of the blood vessels inside the brain using MRA, source: *MR Images Produced at MARIARC*, Liverpool University, UK.

Computed Tomography Angiography (CTA, cardiac CT, cardiac CAT) [16] (see Figure 1.6) is a non-invasive imaging technique, which uses advanced CT technology and produces high resolution images of moving heart and arteries. It is a widely used technique in cardiac imaging, since it provides physicians visualization of 3D heart and arterial anatomy, as well as plaque or calcium deposits in the artery walls. In addition, CTA image acquisition is faster than the other techniques (typically takes less than a minute). During CTA, beams of x-rays are generated from an X-ray source, which rotates around a volume of interest of the patient's body. From several different angles, attenuated x-ray beams are picked up by detectors in the scanner to obtain projection images, from which, 3D attenuation volumes, i.e the CTA image is reconstructed. Although it is not as safe as MRA, it is safer

than invasive techniques since duration of exposition is much less. In this thesis, CTA is the imaging modality of interest because of several mentioned advantages over other modalities.

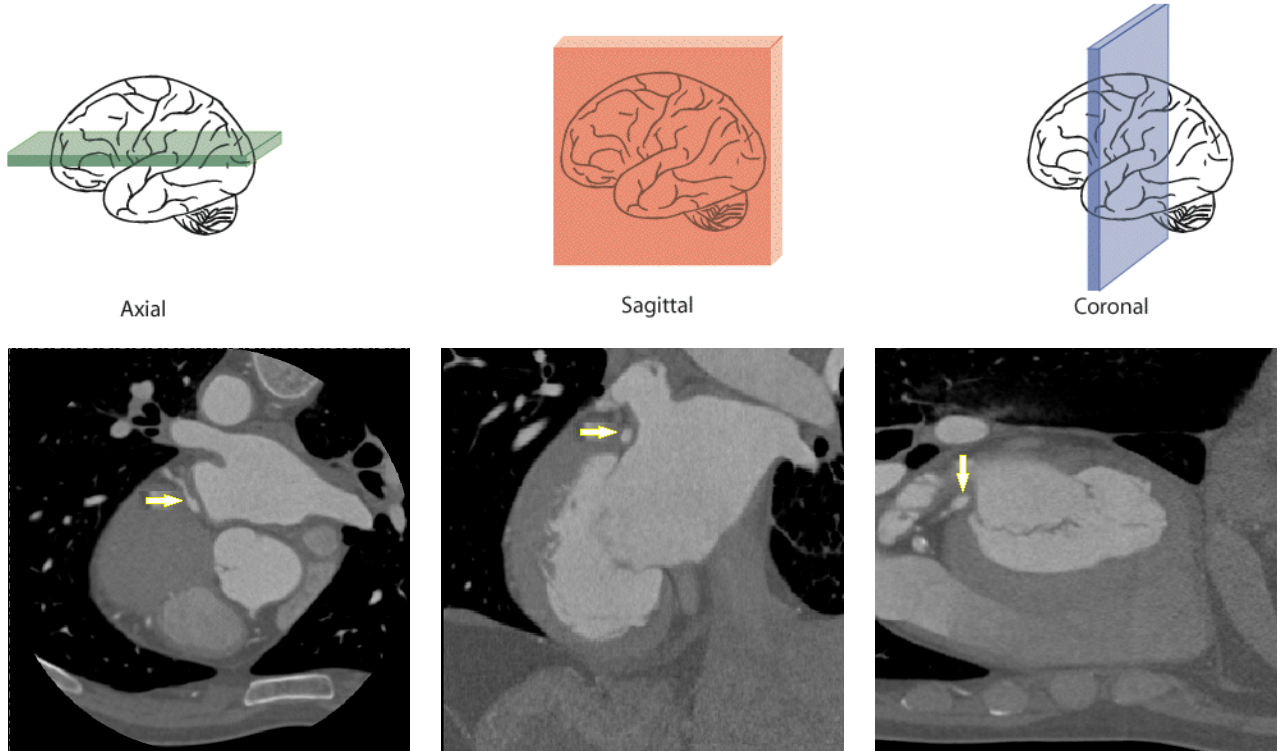


Figure 1.6: Top: Anatomical planes (axial, sagittal and coronal) [3] are shown inside the brain. Bottom: Cardiac CTA images. Arrows indicate LCA in (a) axial view; (b) sagittal view; (c) coronal view.

1.2 Contributions

The complex tubular structures of arteries due to branchings and pathologies make the segmentation of coronary arteries a tough problem in medical image analysis. The structures of arteries become even more complex with stents, calcifications and pathologies such as stenosis. Besides anatomical artifacts, several imaging artifacts occur during acquisition such as noise, contrast and resolution artifacts, which make the problem more challenging. In this thesis, we aim to extract coronary arteries from Computed Tomogra-

phy Angiography (CTA) scans and create geometric model of arteries, which may be used as a medical navigation system to detect possible anomalies on arteries.

To achieve this goal, we design a novel tubular structure segmentation method, which constructs an intensity-based tensor that fits to a vessel, which is inspired from diffusion tensor image (DTI) modeling¹ [17]. The thesis makes several contributions, which can be summarized as follows:

- The anisotropic tensor inside the vessel drives segmentation analogously to a tractography approach in DTI.
- We develop an unsupervised branch clustering method, which can automatically locate multiple branchings on complex tree structures.

Beside several contributions, our approach provide many advantages, where major two advantages can be expressed as follows:

- Our approach is capable of finding the vessel orientation, centerline (central lumen line) and its thickness, i.e. vessel lumen diameter, at the same time.
- The vessel extraction is initialized with a single seed point and an entire coronary artery tree can be captured by an automatic branch detection algorithm.

1.3 Thesis Outline

This thesis is organized as five chapters including the Introduction chapter. In Chapter 2, a background on state-of-the-art literature on vascular segmentation techniques and diffusion tensor imaging (DTI) are presented. Proposed tubular structure segmentation method is presented in Chapter 3. The experimental results are provided in Chapter 4. In the last chapter, the conclusions and future work are presented.

¹A preliminary version of this work is published at "The MICCAI'11 Workshop on Computing and Visualization for (Intra)Vascular Imaging (CVII)" [17].

Chapter 2

Background on Vasculature Segmentation and DTI

2.1 A Brief Review on Vasculature Segmentation Algorithms

Recent developments in imaging technology lead to acquisition of high resolution medical images. Combination of modern mathematical and imaging techniques motivated generation of computer-aided image processing algorithms to delineate anatomical structures in high resolution images. These algorithms, called image segmentation algorithms, play a vital role in numerous biomedical imaging applications such as diagnosis assistance, treatment, quantification of volumes, localization of pathology, study of anatomical structures, surgery planning, and tracking/monitoring of diseases. [18, 19, 20].

Various approaches depending on different classification schemes were proposed as solutions to the problem of segmentation. However, there is no standard segmentation technique that works for all variety of image applications. The commonly used segmentation methods include [21, 22]:

- Active Contours;
- Split and Merge;
- Mean shift and Mode finding;
- Normalized cut;
- Graph cuts and Energy based methods, and so on.

These algorithms can work well on various problems. On the other hand, delineation of vascular structures from inhomogeneous volumes such as these involved in as CT is

problematic, since the intensities inside vessels such as coronary arteries, have variations and noise. Furthermore, since the anatomy of vasculatures (arrangement of blood vessels in body) can vary from person to person, it is hard to create an atlas, which can guide the segmentation process.

Segmentation of vascular structures is a fundamental step for accurate visualization and quantification of pathologies on vessels. Unfortunately, the segmentation still heavily relies on manual operations. Thus, it can take several hours for the physicians to do manual segmentation for a single MRA or CTA dataset. For this purpose, various sophisticated vascular segmentation algorithms are developed. This chapter reviews algorithms developed for segmenting vasculature, especially coronary arteries segmentation from CTA images.

In the first part of this chapter, first, we discuss several filtering approaches. Second, various vessel centerline extraction schemes, which basically can be divided into four, as follows: thresholding and region growing; morphology; minimal-path techniques; model-based approaches, are explained. It should be noted that there are other criteria that can be chosen in order to classify existing algorithms such as: it is automatic or manual; is based on centerline or whole-vessel segmentation; is a general segmentation method or an organ specific segmentation method, etc. The following text describes only a small part of the existing methods for each category. There are several crucial approaches based on ridge traversal [23], gradient vector flow [24] and probabilistic tracking [25], which are not explained in this text. Once and for all, we discuss about the branch detection techniques, and we conclude vasculature segmentation review part of this chapter.

In the second part, we present DTI in order to give the insight of a tensor model we will develop, which is inspired from the DTI tensor model. First, MRI (Magnetic Resonance Imaging), which is the core of DTI, then DTI is explained respectively.

2.1.1 Filtering

Some of the vessel segmentation algorithms use filters to segment vascular structures, or only use them as a prefilter for vessel enhancement before segmentation. Most well-known filtering techniques are subtraction, Hessian-based, non-linear diffusion, and flux-based

filtering.

Subtraction filtering is one of the simplest technique used for filtering. It removes undesired structures in either of two ways: subtracting a template (mask) image from the image to be processed, which is mostly used to enhance blood vessels by removing undesired bone or soft tissue structures from an image; subtracting certain structures such as the heart in an image.

2.1.1.1 Hessian Based Filtering

The second filtering method, Hessian-based filtering is the most popular vessel enhancement technique in the literature, which is based on the analysis of eigenvectors and eigenvalues of the Hessian matrix. Hessian-based filters calculate 2nd order derivatives of the image at each voxel in order to build the Hessian matrix \mathbf{H} . The eigenvalues λ_1 , λ_2 and λ_3 and eigenvectors \mathbf{v}_1 , \mathbf{v}_2 and \mathbf{v}_3 are found by a matrix eigen decomposition of \mathbf{H} , which is computed at each voxel. The eigenvalues and eigenvectors are then used to determine whether the voxel belongs to a tube-like structure.

Koller et. al. [26] were the first to propose to analyse the Hessian matrix to produce “vesselness” measure. Frangi et. al. [12] introduced the vesselness measure based on eigenvalues extracted from the Hessian matrix in a multiscale fashion. The vesselness measure can be analysed based on the hypothesis that the ideal tubular-structure in a 3D image satisfies three criteria:

- 1) $|\lambda_1| \approx 0$;
- 2) $|\lambda_1| \ll |\lambda_2|$;
- 3) $|\lambda_2| \approx |\lambda_3|$.

where the eigenvalues are ordered as $|\lambda_1| \leq |\lambda_2| \leq |\lambda_3|$.

Table 2.1 summarizes the relations that must hold between the eigenvalues of the Hessian for the detection of different structures.

In the case of bright vessels on a dark background such as blood vessels on CTA images, the eigenvalues $(\lambda_1, \lambda_2, \lambda_3)$ appear to be $\lambda_1 \approx 0$, $\lambda_2 \approx \lambda_3 < 0$ and $|\lambda_1| \ll |\lambda_2|$.

Hessian-based filtering is extended by [12] in a multi-scale framework and multi scale

Table 2.1: List of possible patterns in 2D and 3D, depending on the value of the eigenvalue. H: high, L: low, +/- indicate the sign of the eigenvalue [12].

2D		3D			orientation pattern
λ_1	λ_2	λ_1	λ_2	λ_3	
L	L	L	L	L	noise, no preferred direction
		L	L	H-	plate-like structure (bright)
		L	L	H+	plate-light structure (dark)
L	H-	L	H-	H-	tubular structure (bright)
L	H+	L	H+	H+	tubular structure (dark)
H-	H-	H-	H-	H-	blob-like structure (bright)
H+	H+	H+	H+	H+	blob-like structure (dark)

vesselness measure at voxel \mathbf{x} in an image is expressed as:

$$V(\mathbf{x}) = \max_{\sigma} v(\mathbf{x}, \sigma), \quad \sigma \in [\sigma_{min}, \sigma_{max}] \quad (2.1)$$

where v represents a vesselness response, σ indicates the scale of Gaussian derivatives to calculate Hessian matrix. v is calculated in a range of $[\sigma_{min}, \sigma_{max}]$, where calculated maximum vesselness response for each voxel results in a vessel enhanced image:

$$v(x, \sigma) = \begin{cases} (1 - \exp(-\frac{R_A^2}{2\alpha^2})) \exp(-\frac{R_B^2}{2\beta^2}) (1 - \exp(-\frac{S^2}{2c^2})) & \text{if } \lambda_2 \leq 0 \text{ and } \lambda_3 \leq 0, \\ 0 & \text{otherwise} \end{cases} \quad (2.2)$$

In Eq. (2.2), R_A is able to discriminate tubular structures from plate-like structures, R_B mainly differentiates blob-like structures from other structures and also favors tubular structures, and S penalizes random background noise, which are mathematically defined as follows:

$$R_A = \frac{|\lambda_2|}{|\lambda_1|}, \quad R_B = \frac{|\lambda_1|}{\sqrt{|\lambda_2\lambda_3|}}, \quad S = \sqrt{\sum_{1 \leq i \leq 3} \lambda_i^2} \quad (2.3)$$

α , β and c are constants that control the balance between the three terms. Typically, $\alpha = 0.5$, $\beta = 0.5$, and $c = 10$ for the vessels on CTA images.

Following the multi-scale vessel enhancement idea, several algorithms have been proposed in literature [27, 28, 12, 29, 30], which are based on the eigen-analysis of the Hessian

matrix \mathbf{H} .

2.1.1.2 Non-linear Diffusion Filtering

Another popular filtering technique, non-linear diffusion filtering [31, 32] aims to enhance an image by removing noise without removing significant parts of the image as edges, lines and flow-like structures. As compared to the Hessian-based filters, these filters consider the direction of the neighbouring voxels as well as the local direction. As multiscale Hessian-based vessel enhancement filters, diffusion filters create scale-space of images by convolving the image with a Gaussian filter in different σ values.

In scale space theory, the diffusion equation is expressed as

$$\partial_t u = \text{div}(\mathbf{D} \nabla u) \quad (2.4)$$

where ∇u indicates concentration gradient, and $u : \mathbb{R}^m \rightarrow \mathbb{R}$, e.g. here u is a 3D image function with $m = 3$. $\mathbf{D} : \mathbb{R}^m \rightarrow \mathbb{R}^{m \times m}$ represents the diffusion tensor of dimension m , which controls the diffusion flow. When \mathbf{D} is identity, Eq. (2.4) becomes heat equation as $\partial_t u = \text{div}(\nabla u) = \Delta u$.

Multidimensional flux-based anisotropic diffusion filtering is proposed by Krissian et. al. [33]. The diffusion flux is decomposed in a 3D orthogonal basis that depicts the directions of principal curvature, effectively enabling enhancement of contours as well as diffusion along the contour. The diffusion function associated to each vector of the basis depends on the first order derivative of the intensity in this direction, instead of the traditional norm of the smoothed gradient. This may pose a problem along the central axis as the gradient vanishes at these points, possibly leading to undesired behaviour.

Manniesing et. al. [4] proposed a method to enhance vascular structures within the framework of scale space theory. They combined a smooth vessel filter which is based on an analysis of the eigensystem of Hessian, with a non-linear anisotropic diffusion scheme. The amount and orientation of the diffusion depend on the local vessel-likeness. They applied the Vessel enhancing diffusion (VED) to patient and phantom data and compared to linear, regularized Perona-Malik, edge and coherence enhancing diffusion. The method performs better than most of the existing techniques [12, 31, 32] in visualizing vessels in

varying radii and in enhancing vessel appearance. A diameter study on phantom data shows that VED least affects the accuracy of diameter measurements. It is shown that using VED as a preprocessing step improves level set based segmentation of the cerebral vasculature, in particular segmentation of the smaller vessels of the vasculature. In Figure 2.1 the shrinkage effect of the vesselness filter [12] can be observed clearly. As compared to vesselness filter, the shrinkage effect is not present in VED (arrows 1 and 3). Shrinkage appears because of increasing deviation from a tube like structure when approaching the boundaries of the vessel. Furthermore, VED has better performance with respect to background blurring (arrows 2 and 4).

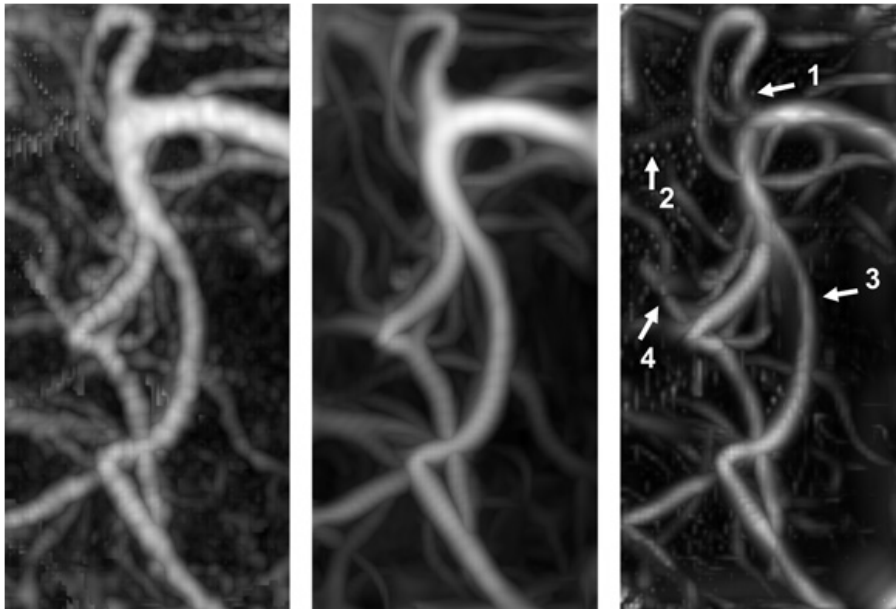


Figure 2.1: A comparison between the VED and Frangi's vesselness filter. The original data is shown in the left figure, the result of VED in the middle figure and the result of Frangi's vesselness filtering in the right figure. Arrows indicate points of interests [4].

Although the VED filter improves the vessel enhancement, there still exist some gaps on discontinuities in 3D-images of tubular structures. Risser et. al. [34] present an algorithm, which merges discontinuities in 3-D images of tubular structures presenting undesirable gaps. The algorithm proposed aims at closing the gaps on the discontinuities. This algorithm is based on the skeletonization of the segmented network followed by a

tensor voting method. It permits to merge the most common kinds of discontinuities found in microvascular networks. It is relatively fast as compared to the VED filter.

2.1.1.3 Other Filtering Methods

Law and Chang [35] proposed a curvilinear structure detector, called Optimally Oriented Flux (OOF), which finds an optimal axis on which image gradients are projected in order to compute the image gradient flux. The computation of OOF is localized at the boundaries of local spherical regions. The main advantage of OOF is its robustness against the disturbance induced by closely located adjacent objects. Moreover, the analytical formulation of OOF introduces no additional computation load as compared to the calculation of the Hessian matrix which is widely used for curvilinear structure detection.

Lesage et. al. [36] proposed geometric and appearance flux-based vessel enhancement model with two features for 3D vascular tracking. The first one, Flux, is formulated as the measure of inward gradient flux through a local circular cross-section. The second one, MFlux, introduces a non-linear component to reduce false positive responses in situations such as step-edges. They compared the cardiac CT data to a selection of published vessel dedicated features. They showed that MFlux induces a particularly discriminative response landscape, which is a desirable property for tracking purposes on such large search spaces.

2.1.2 Vasculature Segmentation Algorithms

Vasculatures are the arrangement of blood vessels, which include blood vessels, coronary artery, neurovascular structures, and so on. To the best of our knowledge, several reviews have been published to segment vasculatures in literature [37, 38, 39, 40, 41, 42, 43]. The first most general and extensive vasculature segmentation survey was published by Kirbas and Quek [37], where they extensively categorized existing methods with respect to their mathematical framework. Other existing reviews focus on specific applications as Peripheral CTA (Felkel et. al. [38]), MRA (Suri et. al. [39, 40]). A more comprehensive review was published by (Buhler et. al. [41]), which covers skeletonization algorithms and visualization techniques. In the most recent review on vascular segmentation, Lesage

et. al [42] presented their analysis on three axes: (i) models (prior assumptions made on the target vessels, e.g. elongation and hyper-intensity); (ii) image features (estimate the models on the image, e.g local intensity curvatures); (iii) extraction schemes (algorithmic core of a vascular segmentation method).

2.1.2.1 Thresholding and Region Growing

Thresholding approaches segment images by partitioning image intensities. It is simple and mostly effective on the images that have contrast in the structures. Advanced thresholding techniques use expectation maximisation [6] or adaptive region growing [44], and similar algorithms. Thresholding is mostly used as a preprocessing. It has several disadvantages as: it does not take into account the spatial characteristics of an image and it is very sensitive to noise and intensity inhomogeneities, which often occur in medical images.

Region growing approaches initialize from a seed point, then incrementally recruit voxels based on some criteria. These criteria are mostly based on intensity similarity and spatial proximity. The major drawbacks of region growing are: it requires user-selected seed points and it is very sensitive to noise and intensity variations.

2.1.2.2 Morphology

Another approach for vessel segmentation is provided by mathematical morphology, which analyses images or objects by their interaction with shapes. Morphological operators are applied to images with basic shapes called structuring elements; they were first defined for binary images, then extended to grey-level images. Erosion and dilation are the two main operations for constructing morphological operators, such as openings, closings and hit-or-miss transforms. A precise definition of morphological operators can be found in [45].

In particular, mathematical morphology operators that have been involved in vessel segmentation methods include: watershed transform [46, 47], grey-level hit-or-miss transform [48], or connected filtering based on component-trees [49, 50]. The usefulness of such operators is justified by their intrinsic capacity to model morphological information, and

then to enable anatomical knowledge-guided approaches. Bouraoui et. al. [51] presented an algorithm, which relies on the blur grey-level hit-or-miss transform with an extension of the blur binary hit-or-miss transform [52].

The advantage of morphology based vessel segmentation algorithms is that they are mostly automatic. However, surrounding structures around the vessel can be detected as vessel and they do not perform well for noisy images.

2.1.2.3 Minimal Path Techniques

Deschamps and Cohen [53, 54, 55] reformulate the problem of centerline extraction as a problem of finding the minimal paths in 3D images. The minimal path technique proposed by Cohen et al. [56] captures the global minimum curve of an active contour model's energy between two points initiated by the user. By defining the image as an oriented graph characterized by its cost function (or potential), the centreline extraction problem turns to be an optimisation problem. This provides the global minimum of the energy function, which avoids the local minima problem as in deformable models. The minimal path approach has several advantages over existing methods such as finding global minima, fast computation, and ease of implementation. Unfortunately, there also exist some disadvantages of minimal path techniques as: vessel boundary extraction is mostly difficult, the path given by minimal path techniques does not always give a correct centerline and minimal path technique only provides a trajectory, does not give information about the vessel boundary and local width.

Minimal path techniques are commonly employed in interactive frameworks, requiring the start and end points for each vessel. Some works have proposed the definition of termination criteria to automatically stop the path propagation and relax the need for end points. For instance, Gulsun and Tek [57] proposed such criteria through heuristic thresholds.

Li and Yezzi [5] proposed a new variant of the traditional, purely spatial minimal path technique by incorporating an additional non-spatial dimension into the search space. They modeled the vessel as a 4D curve (after adding the extra dimension for the 3D image), which consists of three spatial coordinates and extra non-spatial dimension, which

describes the thickness at the corresponding 3D point (see Figure 2.2). Thus, each 4D point represents a sphere in 3D space, and the vessel is obtained as the envelope of the family of spheres traversed along this 4D curve. Li and Yezzi created potentials, which forces the spheres on the detected path to be tangential to the vessel boundary. The centerline of the path is then extracted by tracing the center points of the estimated family of 3D spheres. However, since Li and Yezzi [5] proposed isotropic metrics for potentials, they did not take into account the vessel orientation.

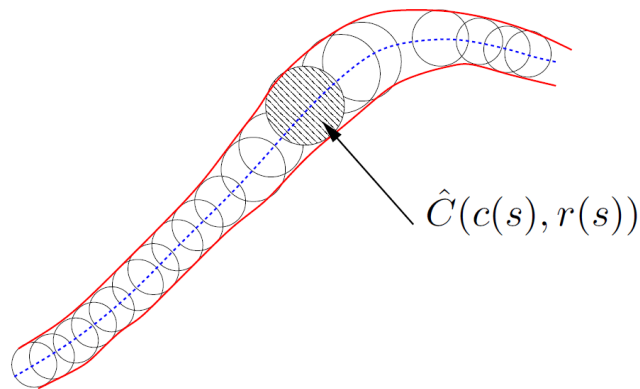


Figure 2.2: A tubular surface is represented as the envelope of a family of spheres with continuously changing center points and radii [5].

To improve this method, Mohan et. al. [58] suggest a minimal path algorithm by using the 4D minimal path model of Li and Yezzi [5]. As they added the extra dimension to the 3D spatial coordinates (the radius dimension), they associated to the path an anisotropic potential related to the Finsler metric. An important contribution of Mohan et. al. is that they considered the orientation of the vessel in their energy function.

Benmansaour and Cohen [59] proposed an interactive vessel segmentation method, which is also based on the minimal path formulation and anisotropic enhancement. Their minimal path formulation is inspired from Li and Yezzi's 4D Curves [5], but they take into account the vessel orientation by considering anisotropic metrics. Their anisotropic

metric is based on the Optimally Oriented Flux (OOF), introduced by Law and Chung [35], by using its scalar function as well as its orientation, which makes the propagation faster along the vessel’s centreline for exact scale (radius).

2.1.2.4 Model-based Techniques

In model-based approaches, explicit vessel models are applied to extract the vasculature. We divide model-based approaches into three categories: (1) Deformable models, (2) Parametric models, (3) Tubular/Cylinder Model. In the next subsections, each category is discussed and the techniques in each category are explained briefly.

Deformable models:

Deformable model approaches have been applied to three dimensional vascular segmentation. In such methods, an initial boundary estimate is deformed iteratively to optimize an energy function which depends both on image information and on the smoothness of the surface. One such algorithm is called snakes (active contours). Another volumetric deformable model approach is based on a level-set representation, which is independent of parametrization of the evolving surface model.

Level Set technique is proposed by Osher and Sethian [60], which is based on an implicit surface that evolves according to geometric and image-based forces in order to adapt to structures in the image. Its main idea is to represent evolving curves as the zero level set of a higher dimensional level set function. The first major advantage of the level set method is that it does not suffer from a parametrization problem, since it is implicit. The second one is, while the level set function evolves over time, its zero level set changes topology; it can split and merge or form sharp corners. Therefore, the level set is useful in segmenting inhomogeneous vascular objects as blood vessels. However, sometimes the level set can leak when it does not contain geometrical constraints in the level set function evolution. For more details, refer to [61]. Figure 2.3 depicts the segmentation of a vessel using a level set function implemented in [6].

There are several level-set based algorithms proposed [62, 63, 64] for vasculature segmentation. For instance, Lorigo et. al [62] proposed *Curves* technique with a two level-set

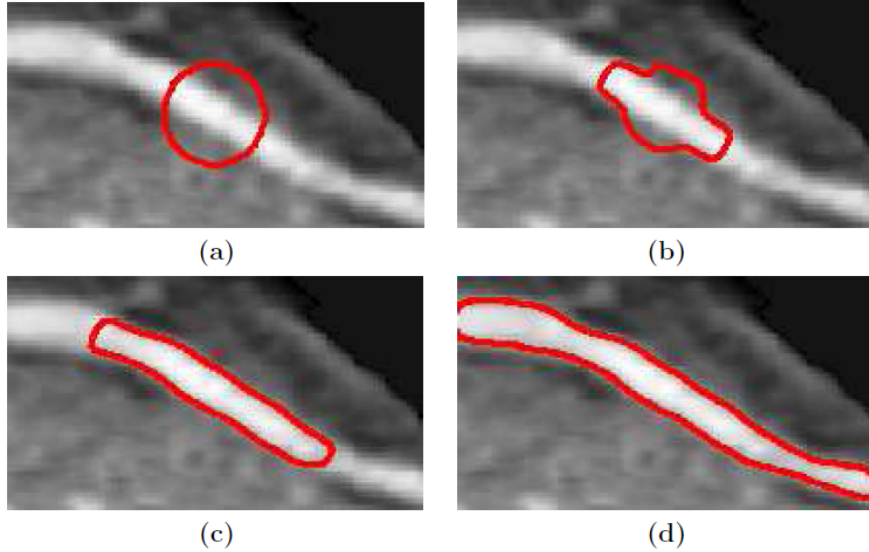


Figure 2.3: Level set segmentation [6]. (a) Initial contour; (b) after 150 iterations; (c) after 600 iterations; (d) after 1600 iterations.

scheme, which has principle of evolving a 1D curve on a 3D domain. *Curves* evolves a width-limited surface, called ϵ -levelset. A new energy term constrains the lowest curvature of this surface, which is proved to show the vessel’s principal direction.

Blood vessels are challenging structures to segment due to the branching and thinning as well as the decrease in image contrast from the root of the vessel to their thin branches. It causes leakages, when the image intensity is used alone to guide the deformable models where the image information is ambiguous. To address this problem, Nain et. al. [7] presented a deformable segmentation method for vessels using an implicit deformable model with a soft shape prior. They combined image statistics and shape information to derive a region-based active contour that segments tubular structures and penalizes leakage. Figure 2.4 shows their coronary artery segmentation results for a CTA dataset.

Tubular/cylinder and elliptical cross-sectional models:

Friman et. al. [65] proposed a tubular tracking algorithm based on 3D template matching, called Multiple Hypothesis Tracking (MHT) framework, which is used to traverse difficult vessel passages such as pathologies and areas of low contrast. The algorithm

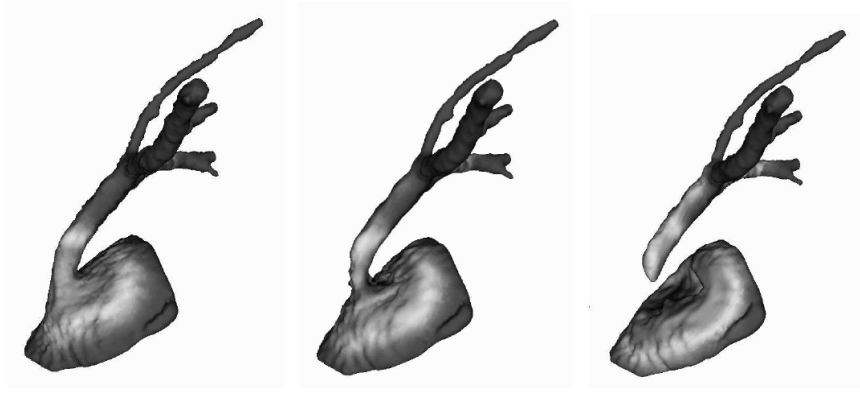


Figure 2.4: Segmentation of coronary arteries from CTA data [7]. Left: Initial - deformable model based only on image intensities, the artery leaks into aorta; Middle: Deformable model based on image intensities and shape prior (after 400 iterations - artery is disconnecting from aorta); Right: Deformable model based on image intensities and shape prior (after 800 iterations - the artery totally disconnected from aorta).

starts from an initial point given on the centerline, a search tree is built by recursively evaluating possible vessel continuations. Sometimes MHT can terminate earlier; in this case, a minimal path algorithm based on Fast Marching is needed to fill the gaps between newly initialized points and terminated points. The vessel template model presented in [65] has a flatter vessel profile than the Gaussian profile used in [66], and provides flexible central position, radius and orientation adjustment. Worz et. al. [8] proposed tubular vessel models of varying sizes using a Gaussian smoothed 3D cylinder, since the 2D cross-sections of medium and large sized vessels is plateau-like (see Figure 2.5) and cannot be accurately represented by a 2D Gaussian profile.

Although circular models are widely used to represent vessel cross-sectional shapes, sometimes the circular models are insufficient in representing non-circular sections. Tyrell et. al. [9] proposed a cylindroidal superellipsoid model to represent complex vasculature in 3D images. This model locally describes the vessel in combination with a constant intensity appearance model. (See Figure Figure 2.6)

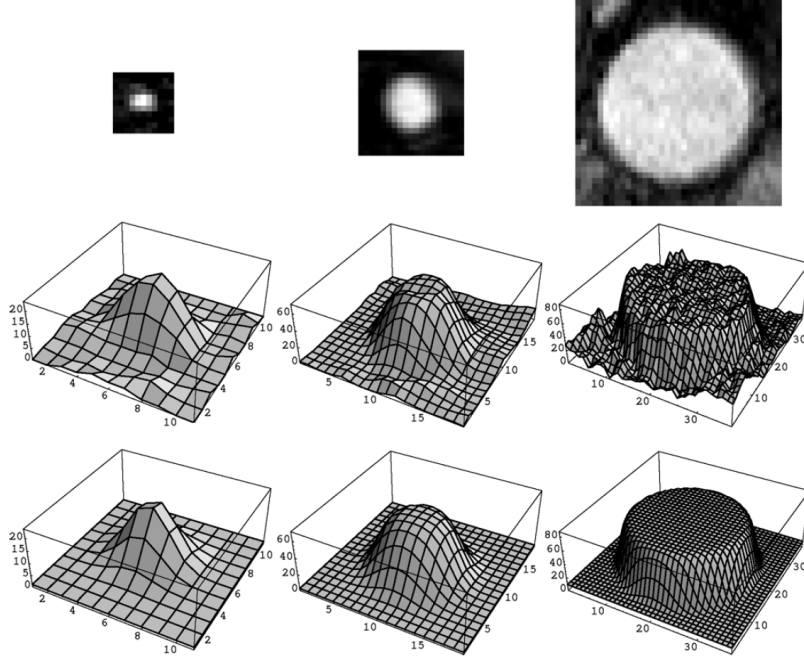


Figure 2.5: Intensity plots of orthogonal 2-D slices; Left: a thin vessel in the pelvis, Center: the artery iliaca communis, and Right: the aorta; Top: 2D cross-section from MR images, Middle: Intensity profile of slices, Bottom: 2-D sections of generated 3-D images using the new cylindrical intensity model [8].

2.1.3 User Interaction

Creating a robust fully automatic vessel extraction algorithm is one of the most challenging and ongoing problems in literature. Most methods require some user interaction at least for the final verification of results. According to the amount of interaction, methods can be classified into three categories: fully automatic, semi-automatic, or interactive.

Fully automatic algorithms require only the input data and do not need any user interaction during the segmentation process, e.g. [67]. On the other hand, interactive algorithms require user guidance during the segmentation process, e.g [68], which can be time-consuming and rely on the skill of users. Semi-automatic algorithms [7] mostly require start and end points for each branch to start the segmentation. Contrary to the interactive methods, semi-automatic methods mostly do not need any user interaction during the segmentation process. Most of the segmentation algorithms are semi-automatic or

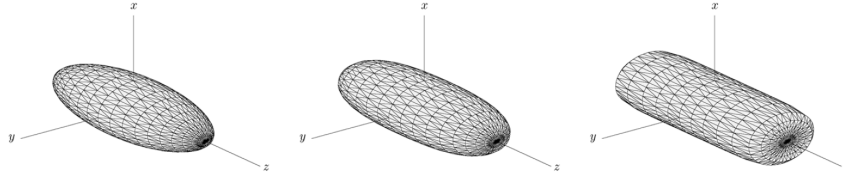


Figure 2.6: Superellipsoid models with varying parameter ϵ_1 [9]. Left: $\epsilon_1 = 1.0$; Middle: $\epsilon_1 = 0.75$; Right: $\epsilon_1 = 0.25$.

interactive, which require various levels of interaction to start and guide the segmentation.

2.1.4 Branch Detection

Fully automatic vessel extraction algorithms as [67, 24] implicitly deal with branching. Interactive methods mostly do not handle branching, since user interaction is provided for every branch. Some semi-automatic methods explicitly represent bifurcations [69] or others perform vascular tree connection after finding the branches [58]. For instance, Mohan et. al. [58] suggested a K-means clustering algorithm with an assumption that vessels have at most two branches to be separated. Li et. al. [70] proposed to use a 4D interactive key point searching scheme. After the key points are located, iteratively, the branches are identified by finding structures between all adjacent key point pairs.

2.2 DTI (Diffusion Tensor Imaging)

Our novel vasculature segmentation technique is based on an intensity-based tensor model that represents a vessel, which utilized ideas from diffusion tensor image (DTI) modeling. In order to give the insight of our method, DTI is briefly presented in this part of the chapter. First, MRI (Magnetic Resonance Imaging), which is the core of DTI, is explained.

2.2.1 Magnetic Resonance Imaging (MRI)

Magnetic resonance imaging (MRI) is a non-ionizing technique with excellent soft tissue contrast. However, it is a much slower technology than other imaging techniques

as ultrasound, and computed tomography (CT), since the scan times range between 3-10 minutes. MRI is mainly used in the brain diseases, spinal cord disorders, musculoskeletal damage; also, in angiography, and cardiac imaging.

According to classical theory of MRI, source of the MRI signal is nucleus of hydrogen, which spins and causes a magnetic field, called, magnetic moment (see Figure 2.7). Owing to the influence of external magnetic field, nuclei produce a secondary move, called precession (see Figure 2.8). The frequency of precession is directly proportional to strength of external magnetic field. In an ordinary environment, magnetic moments of each nucleus are jumbled about in all directions, so that the sum of all magnetic moments, called net magnetization vector (NMV), is approximately zero. However, in an external magnetic field magnetic field of protons are aligned either parallel or anti-parallel to the direction of external magnetic field [10].

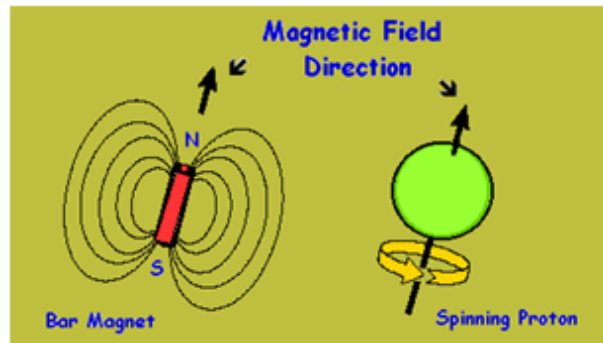


Figure 2.7: Magnetic moment of a proton, source: *"Basic Physics of Nuclear Medicine/ MRI & Nuclear Medicine"*, wikibooks.

Since radio frequency (RF) signals of the nuclei with even numbered particles cancel each other, only the nuclei having odd atomic mass number contribute to MR signal. There are various active elements such as hydrogen (^1H), fluorine (^{19}F), phosphorous (^{31}P), nitrogen (^{15}N), and sodium (^{23}Na). Hydrogen is the element used in MRI due to having a single proton with a large magnetic moment, and existing in large numbers inside human body .

The frequency or speed of precession of the nuclei in a specific external magnetic field strength is expressed using Larmor equation as $\omega_0 = \gamma B_0$, where γ is the gyromagnetic

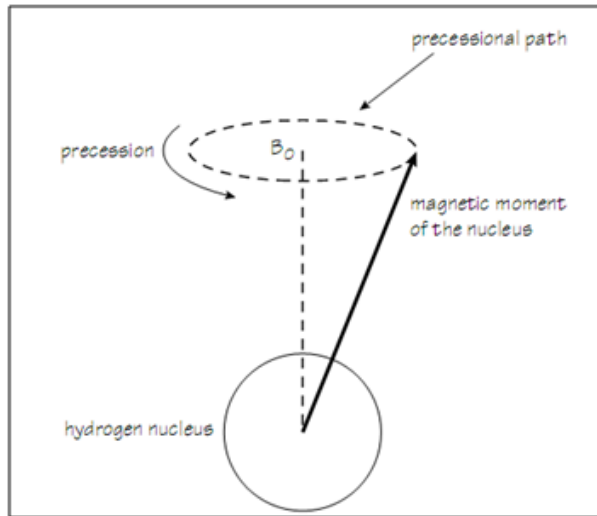


Figure 2.8: Precession [10].

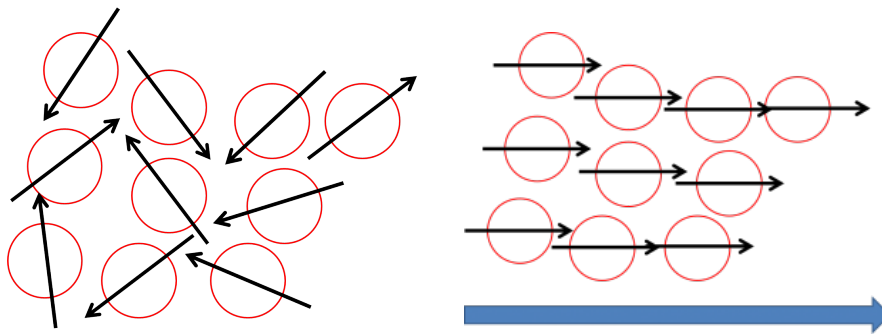


Figure 2.9: Illustration of magnetic moment applied; Left: before; Right: after.

ratio and the precessional frequency of a specific nucleus at 1 T and has units of MHz/T. As it is constant, precessional frequency ω_0 is directly proportional to the strength of external magnetic field B_0 .

Resonance is defined as the energy transition that occurs when an object is excited with a frequency the same as its own. In MRI, resonance could be induced by applying radio frequency pulses, because the precession frequency of the hydrogen (42.57 MHz/T) nuclei is low and it carries small amount energy similar to radiowaves [10]. MR signal is detected using this technique, that is, applied RF pulses cause a change in the NMV, and this change induces a voltage in the receiver coils. In order to construct an anatomical image, sequences of RF pulses called pulse sequences are used to excite protons.

2.2.2 Diffusion Tensor Imaging (DTI) basics

MRI diffusion is based on random thermal (Brownian) motion of water molecules. In the presence of strong diffusion gradients, MR signal is decreased as a result of the dephasing of spin coherence [71]. If spins do not make any movement, gradient pulses cancel out each other; meanwhile, moving spins experience phase shift. Therefore, signal attenuation occurs in normal tissues with random motion, and high signal appears in restricted diffusion [10].

The amount of attenuation depends on the amplitude and direction of applied diffusion gradient. In order to produce diffusion weighted images, magnetic field gradients (diffusion gradients) are applied in certain directions. Strength of diffusion weighting is described by b factor, a parameter that is determined by the shape of diffusion gradient. For the Stejskal-Tanner spin echo sequence (see Figure 2.10), the equation of the sequence is expressed as follows:

$$b = \gamma^2 G^2 \delta^2 \left(\Delta - \frac{\delta}{3} \right) \quad (2.5)$$

where b value is determined by duration δ , G is the strength of gradient pulses, and Δ is defined as the time interval between two gradients and γ is the gyromagnetic ratio [71].

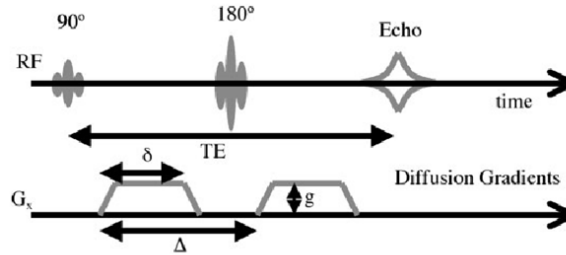


Figure 2.10: Diffusion weighted Spin Echo Pulse Sequence.

The MR signal loss due to strong diffusion gradients could be expressed as in Eq. 2.6, where S is the measured diffusion weighted signal, S_0 is the signal without diffusion gradient, b is diffusion weighting factor, and D is diffusion constant which is also known as apparent diffusion coefficient (ADC).

$$S = S_0 e^{-bD} \quad (2.6)$$

For water at $37^\circ C$ diffusion constant D is approximately $3.210^{-3} mm^2/s$. Diffusion constant may represent the isotropic diffusion for which the diffusion is the same in all directions. However, for a tissue oriented in certain directions such as white matter tracts in the human brain, diffusion is not the same in all directions, thus, the diffusion is anisotropic.

Diffusion is represented mathematically with a 2nd rank, 3 by 3 symmetric tensor (Eq. 2.7), which corresponds to an ellipsoid in three-dimensional (3D) space:

$$\mathbf{D} = \begin{bmatrix} D_{xx} & D_{xy} & D_{xz} \\ D_{yx} & D_{yy} & D_{yz} \\ D_{zx} & D_{zy} & D_{zz} \end{bmatrix}. \quad (2.7)$$

In the case of 3×3 diffusion tensor representation, Eq. 2.6 reexpressed as Eq. (2.8), where $b_0 = \gamma^2 G^2 \delta^2 (\Delta - \frac{\delta}{3})$ and \mathbf{g} is the gradient direction in three-dimensional space:

$$S = S_0 e^{-b_0 \mathbf{g}^T \mathbf{D} \mathbf{g}} \quad (2.8)$$

The most essential information that DTI provides is the orientation of the greatest diffusion at each voxel. It assumes that the largest principal axis of the diffusion tensor aligns with the dominant fiber (white matter tract) orientation in an MRI voxel. In order to find the principal direction of the diffusion tensor, tensor is diagonalized. The eigenvector corresponds to the largest eigenvalue represents the principal direction of the diffusion tensor.

Degree of anisotropy (DAI) of diffusion is measured in different ways. The most widely used DAI is FA (fractional anisotropy) [72], which range from 0 (isotropic) to 1 (fully anisotropic) and is expressed as:

$$FA = \sqrt{\frac{3}{2}} \sqrt{\frac{(\lambda_1 - \bar{\lambda})^2 + (\lambda_2 - \bar{\lambda})^2 + (\lambda_3 - \bar{\lambda})^2}{\lambda_1^2 + \lambda_2^2 + \lambda_3^2}}, \quad (2.9)$$

where λ_1 , λ_2 and λ_3 are the eigenvalues of the diffusion tensor \mathbf{D} , and $\bar{\lambda} = \frac{1}{3} \sum_{i=1}^3 \lambda_i$.

The vessel orientation can be represented better by using red, green, blue (rgb) color channels and weighting the FA with the x, y, z components of principal direction of the tensor, where red color indicates left-to right direction, green anterior-posterior direction and blue represents the superior-inferior direction [72] (See Figure 2.11 for anatomic planes and orientations). Figure 2.12 depicts B_0 image (no diffusion gradients), FA and color- FA maps respectively.

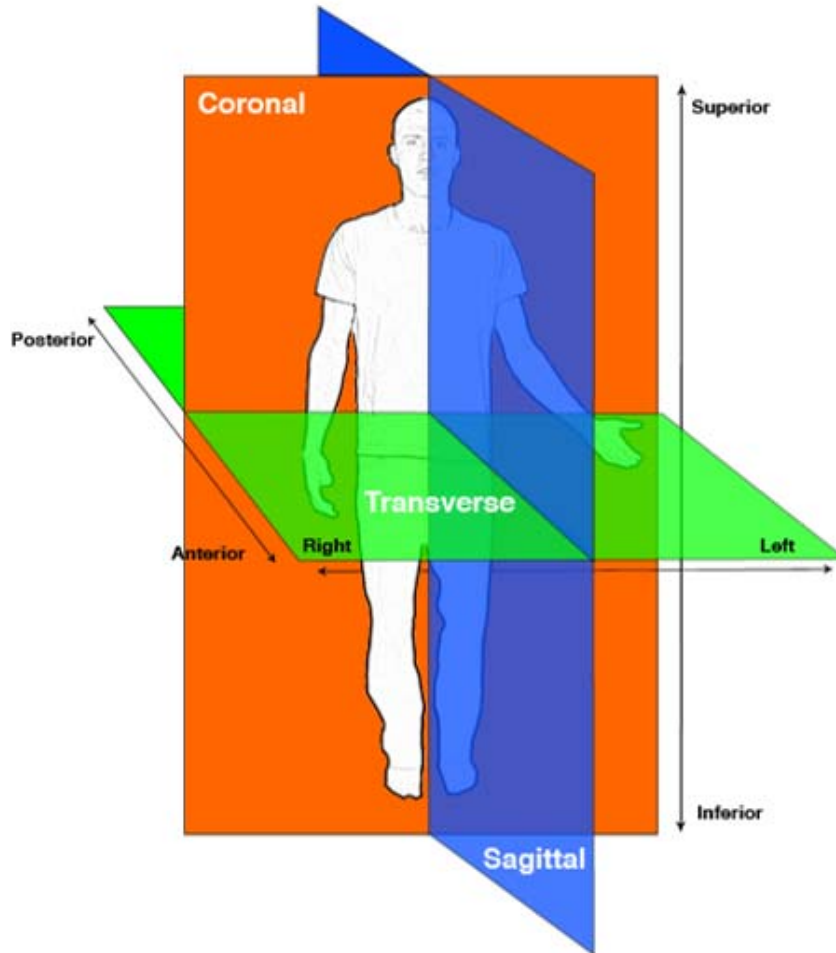


Figure 2.11: The human body can be divided into 3 major planes: coronal dividing the body into anterior and posterior parts, transverse (axial) dividing the body into superior and inferior parts, and sagittal dividing the body into right and left parts. These planes can be moved to any position in the body and are typically used for the tomographic imaging techniques, such as MRI and CT, source: *Anatomy tutorial*, University of Minnesota.

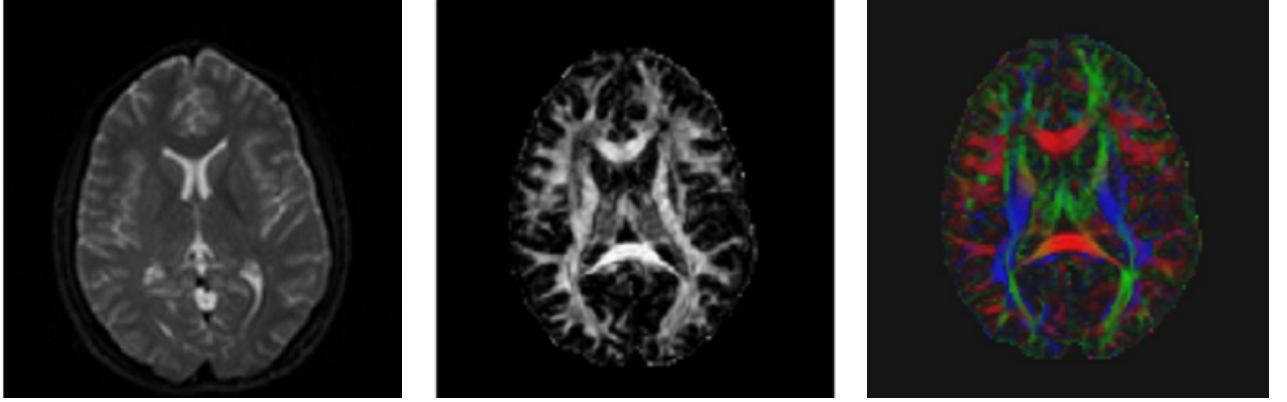


Figure 2.12: Left: B_0 (DTI without gradient); Middle: FA image; Right: Color-FA image.

2.2.2.1 DTI Tractography

DTI Tractography generates fiber tract trajectories in white matter. The conventional white matter tractography reconstructs the pathways of white matter tracts by starting from a seed voxel and tracing down the trajectory in a voxel-by-voxel manner along the principal eigenvector in each voxel. At each voxel, the principal eigenvector \mathbf{v}_1 , which is the one corresponding to the largest eigenvalue λ_1 generated by the decomposition of the diffusion tensor, is aligned with the mean fiber direction in that voxel.

Streamline Tractography (SLT) is the original method of DTI tract estimation and has become a reference of comparison for newer tractography algorithms. Basic Euler's method SLT algorithm is one of the most well-known tractography algorithms in literature [73, 74, 75]. SLT uses the principal eigenvector orientation to compute a Euler's method approximation to the parameterized tract $\mathbf{c}(s)$:

$$\mathbf{c}(s_1) = \mathbf{c}(s_0) + \alpha \mathbf{t}(s) \approx \mathbf{c}(s_0) + \alpha \mathbf{v}_1(s) \quad (2.10)$$

In Eq. (2.10), $\mathbf{c}(s)$ is computed using piecewise linear steps of size α in the direction of the principal eigenvector of the tract. Because the principal eigenvector approximates the true local tangent, $\mathbf{t}(s)$, to the tract curve, tract propagation occurs in both collinear tangent directions approximated by $\mathbf{v}_1(s)$. Tract propagation is subject to stopping criteria which include but are not limited to curvature, torsion, and local anisotropy metrics such as fractional anisotropy.

2.3 Summary

A review of the works on coronary artery segmentation is presented in the first part of the Chapter. The algorithms, which are surveyed, are mostly for static and high-quality CTA or MRA images. Our aim is to give an intuition about different methodologies used for vasculature segmentation, since a few of these methods form the basis of our work.

Recently, creating anisotropic metrics or models has become more popular in vessel extraction. Along this line, we design a novel tubular structure segmentation method, which constructs a plate-like tensor from image intensity measurements to conform vessel cross-sections. Then, motivated by diffusion tensor imaging (DTI) tract following methods, a tractography-like vessel segmentation method is proposed in this thesis. In the second part of this chapter, background on DTI (Diffusion Tensor Imaging) and its principles are given, since DTI forms the basis of our tensor model.

Chapter 3

Vessel Tractography using an Intensity Based Tensor Model

We propose an intensity based tensor model, which is well suited for tubular structures as vessels, by its use of a 4D curve representation, which is inspired from Li and Yezzi’s work [5]. They proposed a 4D curve representation for the vessel-like tubular structures, which has four parameters (\mathbf{X}, r) , where $\mathbf{X} = (x, y, z)$ denotes a centerline point, and r denotes a radius. Each 4D point defines a sphere in 3D space, the path between two 4D points is found by solving a minimal path problem. At the end, the vessel is obtained by connecting the consecutive spheres, where the diameter of the sphere, $2r$, for each 4D point defines the vessel lumen thickness, and the pathway connecting the center of the spheres represents the vessel centerline. Although the method they presented is innovative, their potential metric is isotropic, and, the vessel orientation is not taken into account in this method.

Our novel contributions are three-fold: (1) to bring an anisotropy metric to the potential model by involving potential measurements from intensity at various spatial directions and using them in a linear least squares tensor fitting to estimate a rank 2 tensor; (2) to adapt brain white matter tractography idea for vessel tractography, for the first time to our knowledge; (3) to design a new tubular bifurcation detection algorithm.

Flowchart of the overall algorithm is given in Figure 3.1. The flowchart can be summarized as follows:

- (a) The algorithm is initialized with a user defined point \mathbf{P}_n around the centerline; at the same time, \mathbf{P}_n is added to centerline point list, $List_P$;
- (b) A point \mathbf{P}_n is popped from $List_P$, and set as \mathbf{Seed}_P ;

- (c) Tensors are estimated in a range of radius, and the tensor with the true radius r and the direction of the vessel are estimated at point \mathbf{P}_n by tensor fitting. Then, tractography is started along the direction of the vessel, \mathbf{v} ;
- (d) The point \mathbf{P}_n is centralized and updated;
- (e) The branches around \mathbf{P}_n are searched and detected, and branch coordinates are added to the $List_P$;
- (f) If the mean of the sphere centered at \mathbf{P}_n with radius r is above a given threshold, new point \mathbf{P}_{n+1} is tracked, and the algorithm continues from (b);
- (g) If the mean of the sphere centered at \mathbf{P}_n with radius r is below a given threshold, tract reaches the end of the vessel. The steps after (b) are executed after setting \mathbf{Seed}_P to \mathbf{P}_n whether the negative direction of the \mathbf{v} for the \mathbf{Seed}_p has not been carried out; otherwise, if the list \mathbf{P}_n is not empty, new seed point \mathbf{Seed}_P is selected, and the algorithm starts from (b).

3.1 Image preprocessing

Vessel calcifications are not part of the vessel lumen, for this reason, they are eliminated before the vessel tractography algorithm is applied. The images are prepared for segmentation using a thresholding technique by setting the voxel intensity for vessel calcifications equal to the intensity of the myocardial tissue t_{myo} , which is expressed mathematically as follows:

$$\tilde{I}(\mathbf{x}) = \begin{cases} I(\mathbf{x}) & \text{if } I(\mathbf{x}) \leq t_{calc}, \\ t_{myo} & \text{if } I(\mathbf{x}) > t_{calc} \end{cases} \quad (3.1)$$

where $\tilde{I}(\mathbf{x})$ indicates the preprocessed image produced from the original image $I(\mathbf{x})$ with $x \in \mathbb{R}^3$. The thresholds are fixed to $t_{myo} = 950$ and $t_{calc} = 1700$, which are set in [65].

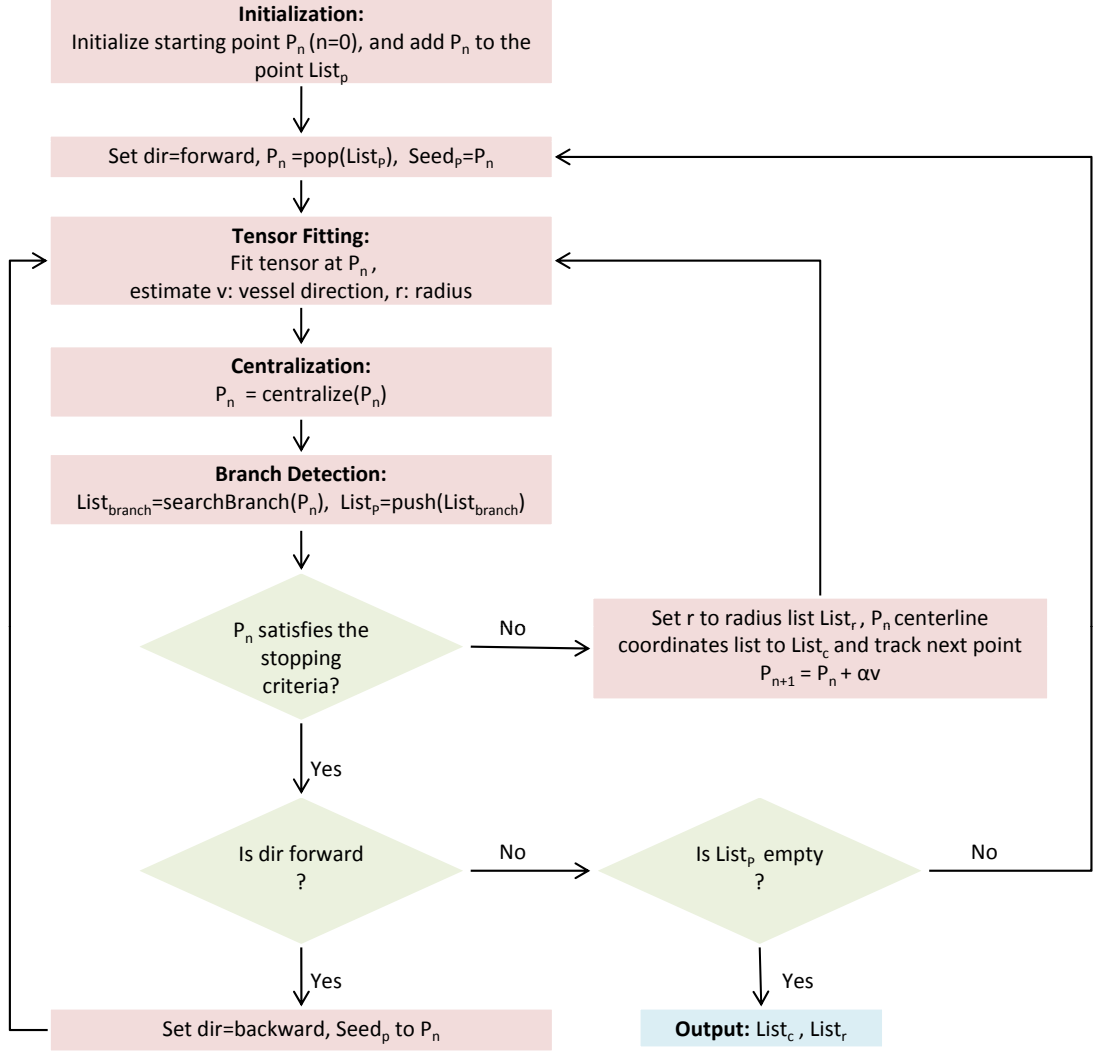


Figure 3.1: Flowchart of the vessel tractography algorithm.

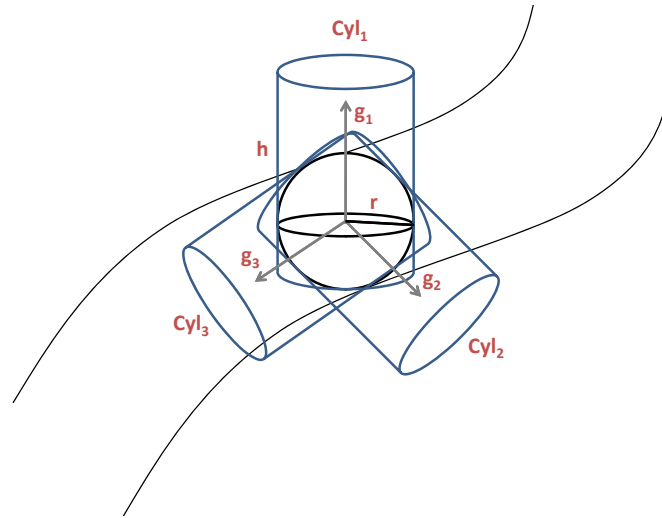
3.2 Intensity Based Tensor Fitting

Our vessel model is constructed as follows:

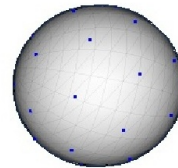
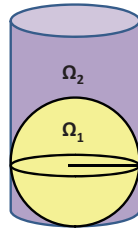
$$\hat{\mathbf{C}}(u) = (\mathbf{c}(u), r(u)) \quad , \quad \hat{\mathbf{C}} \in \mathbb{R}^4 \quad , \quad u \in [0, L] \quad (3.2)$$

where $\mathbf{c}(u)$ represents the location on a vessel centerline in \mathbb{R}^3 , $r(u) \in [r_{min}, r_{max}]$ represents the radius of a sphere centered at $\mathbf{c}(u)$, and L is the length of the vessel. A sphere can be defined at a centerline coordinate point $\mathbf{x}_s \in \mathbb{R}^3$ as: $sph = (\mathbf{x}_s, r)$. A cylinder along each sampled orientation \mathbf{v} is defined as $cyl = (disk(\mathbf{x}_d, r, \mathbf{v}), h)$, where \mathbf{x}_d is defined as a point in \mathbb{R}^2 , \mathbf{v} is an orientation vector in \mathbb{R}^3 , which also indicates the normal

vector of the disk, and $h = 3r$ is defined as the height of the cylinder (Figure 3.2). The orientation vectors are specified by dense sampling over a unit sphere \mathbb{S}^2 . Each potential measurement M_i at a given direction \mathbf{g}_i is an image based feature, which is modeled according to the intensity properties of the vessel. The potential is based on a difference between the intensity mean μ_{Ω_1} of the sphere Ω_1 and intensity mean μ_{Ω_2} of the region Ω_2 , where $\Omega_1 = sph$ and $\Omega_2 = cyl - sph$, and calculated along each orientation vector defined on \mathbb{S}^2 .



(a) Measurements model: Each Cyl_i is characterized by the direction vector \mathbf{g}_i , the height h , and the disk centered at point \mathbf{x}_d with radius r .



(b) Cylinder model;

(c) Orientations on the sphere*;

*Figure from BioImage Suite Tool, Yale University School of Medicine

Figure 3.2: Illustrations of the measurement model, cylinder model, and orientations on unit sphere.

The sketch in Figure 3.2 illustrates the measurement model, a sphere and the cylinders around the sphere in different orientations. Figure 3.2(a) depicts three different orientations $\mathbf{g}_1, \mathbf{g}_2, \mathbf{g}_3$ and the cylinders located along these orientations. The regions Ω_1 and Ω_2 are shown in Figure 3.2(b). The unit orientations on \mathbb{S}^2 are illustrated in Figure 3.2(c). For instance, a few of the sample orientation vectors on the unit sphere are given by:

$$\mathbf{g}_i = \begin{bmatrix} 0.135 \\ -0.986 \\ 0.098 \end{bmatrix}, \text{ or } \mathbf{g}_i = \begin{bmatrix} 0.650 \\ -0.463 \\ -0.603 \end{bmatrix}, \text{ or } \mathbf{g}_i = \begin{bmatrix} -0.206 \\ 0.662 \\ 0.720 \end{bmatrix}, \dots \quad (3.3)$$

Formally, M_i is expressed as follows:

$$M_i = (\mu_{\Omega_1} - \mu_{\Omega_2})^2 \quad (3.4)$$

and measurement orientations are defined as a matrix:

$$\mathbf{G} = \begin{bmatrix} \mathbf{g}_1 & \mathbf{g}_2 & \dots & \mathbf{g}_m \end{bmatrix} \quad (3.5)$$

where $\mathbf{g}_i = [g_{ix} \ g_{iy} \ g_{iz}]^T$ is the column vector for each measurement orientation and m is the number of orientations on \mathbb{S}^2 . M_i can be modelled as $M_i = \mathbf{g}_i^T \mathbf{D} \mathbf{g}_i$ using a 3×3 tensor, which is a symmetric (semi)positive definite matrix:

$$\mathbf{D} = \begin{bmatrix} d_{xx} & d_{xy} & d_{xz} \\ d_{yx} & d_{yy} & d_{yz} \\ d_{zx} & d_{zy} & d_{zz} \end{bmatrix}. \quad (3.6)$$

After the measurements $\mathbf{M}_{m \times 1}$ are calculated for all orientations, the tensor \mathbf{D} is calculated by a least squares fitting as explained next.

To solve for \mathbf{D} from $M_i = \mathbf{g}_i^T \mathbf{D} \mathbf{g}_i$, $i = 1, \dots, m$ equations, we can simply stack the components of \mathbf{D} since \mathbf{D} is a symmetric matrix, as:

$$\mathbf{d} = \begin{bmatrix} d_{xx} & d_{yy} & d_{zz} & d_{xy} & d_{xz} & d_{yz} \end{bmatrix}^T \quad (3.7)$$

and reconstruct the equation as

$$M_i = \mathbf{H}_i \mathbf{d}, \quad (3.8)$$

where \mathbf{H}_i is the i^{th} row of the matrix constructed as:

$$\mathbf{H} = \begin{bmatrix} g_{1x}^2 & g_{1y}^2 & g_{1z}^2 & 2g_{1x}g_{1y} & 2g_{1x}g_{1z} & 2g_{1y}g_{1z} \\ \vdots & \vdots & \vdots & \vdots & \vdots & \vdots \\ g_{mx}^2 & g_{my}^2 & g_{mz}^2 & 2g_{mx}g_{my} & 2g_{mx}g_{mz} & 2g_{my}g_{mz} \end{bmatrix} \quad (3.9)$$

In matrix form, Eq. 3.8 becomes $\mathbf{M} = \mathbf{H}\mathbf{d}$. Linear least squares fitting is applied to solve for \mathbf{d} as:

$$\mathbf{d} = (\mathbf{H}^T \mathbf{H})^{-1} \mathbf{H}^T \mathbf{M}. \quad (3.10)$$

Once \mathbf{d} is obtained, we construct the vesselness tensor \mathbf{D} , simply as in Eq. (3.6).

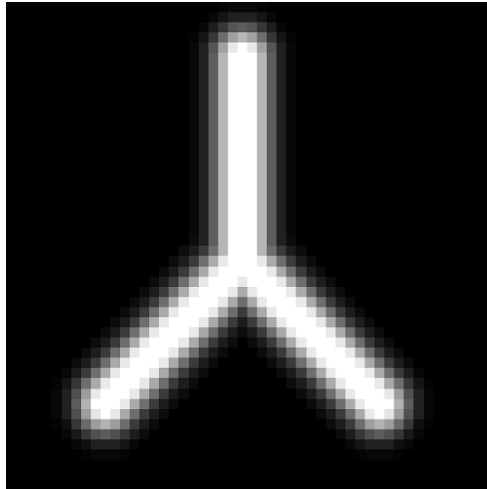
3.2.1 Vessel Lumen Thickness Estimation:

To estimate the final tensor \mathbf{D} , which describes the direction of the vessel and the radius of the sphere, the tensor \mathbf{D}^r is calculated $\forall r \in [r_{min}, r_{max}]$ at a point inside the vessel. When the diameter of the sphere is below or above the vessel lumen thickness, the measurements M_i become lower. The M_i thus becomes largest with the sphere which is tangent to the vessel and, hence the radius of the sphere is detected as:

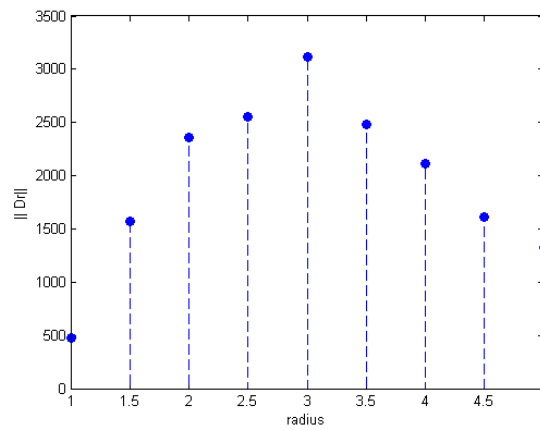
$$\hat{r} = \underset{r}{argmax} \|\mathbf{D}^r\|, \forall r \in [r_{min}, r_{max}] \quad (3.11)$$

where $\|\cdot\|$ denotes 2-norm of the matrix \mathbf{D}^r . That is, the norm of the tensor in Eq. 3.11 happens to be largest when the sphere fits to the vessel boundary. Estimated tensor \mathbf{D} is equal to $\mathbf{D}^{\hat{r}}$. After the tensor \mathbf{D} is computed, it is decomposed into its eigenvalues and eigenvectors using SVD(Singular Value Decomposition): $\mathbf{D} = \mathbf{V} \boldsymbol{\lambda} \mathbf{V}^T$, where $\{\lambda_1, \lambda_2, \lambda_3\}$ are the eigenvalues and $\mathbf{V} = [\mathbf{v}_1, \mathbf{v}_2, \mathbf{v}_3]$ are the eigenvectors of the tensor. Hence, \mathbf{v}_3 represents the smallest eigenvector of the tensor. In Figure 3.3(a), a synthetic Y-shaped vessel data [76] at a constant thickness is shown. Norm of the tensor is plotted as a function of sphere radius in Figure 3.3(b). For instance, the norm at radius 3 becomes maximum for a specific voxel chosen from the centerline of the synthetic vessel.

The tensor \mathbf{D} consists of two major eigenvectors, so it becomes a planar ellipsoid as shown in Figure 3.4. Shape of the tensors on the centerline are more planar and have bigger norm than the others. In addition, when the radius is smaller or larger than



(a) $60 \times 60 \times 60$ synthetic vessel volume with a constant radius of 3.



(b) Norm of the tensor D^r for a voxel on the centerline of the synthetic data, for a range of radius r .

Figure 3.3: Example of vessel lumen thickness estimation.

the true radius, the norm of the tensor becomes lower. Similarly, since the intensity distribution changes less along the vessel direction, the measurements taken through this direction becomes lower, and this tends to have smallest eigenvector in vessel direction. The smallest eigenvector of the tensor \mathbf{D} thus happens to show ultimately the vessel orientation.

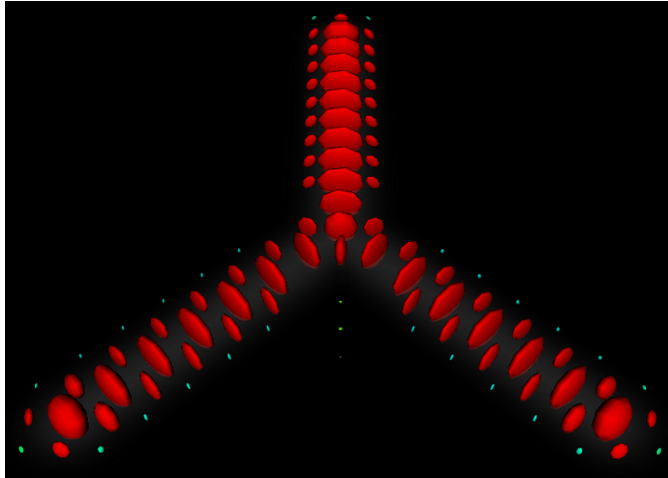
Several anisotropy metrics may be used to measure the anisotropy of a tensor \mathbf{D} . One of the most common way of measuring the anisotropy is fractional anisotropy (FA) [72] which ranges from 0 (isotropy) to 1 (maximum anisotropy), and can be expressed as follows:

$$FA = \sqrt{\frac{3}{2}} \sqrt{\frac{(\lambda_1 - \bar{\lambda})^2 + (\lambda_2 - \bar{\lambda})^2 + (\lambda_3 - \bar{\lambda})^2}{\lambda_1^2 + \lambda_2^2 + \lambda_3^2}}, \quad (3.12)$$

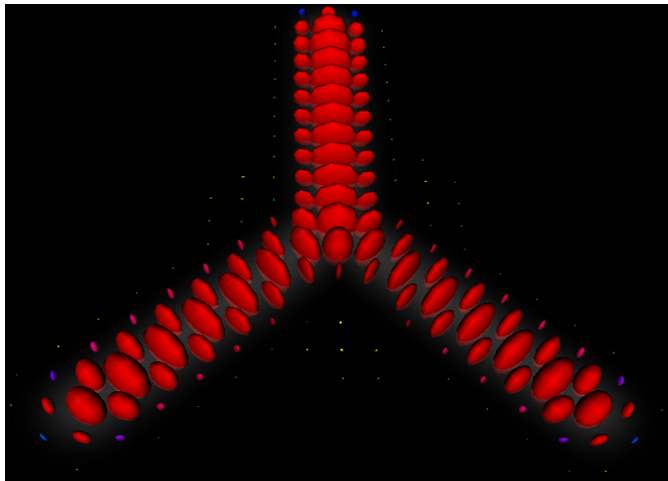
where $\bar{\lambda}$ denotes the mean of the three eigenvalues. The vessel orientation can be mapped by using (red, green, blue)=(rgb) color channels by weighting the FA with the components of $\mathbf{v}_3 = (v_x, v_y, v_z)$ where red color indicates left-to right direction, green anterior-posterior direction and blue represents the superior-inferior direction (See Figure 3.5-Right). In Figure 3.5-Left, a color-FA map represents the v_3 vector orientation of the synthetic Y dataset with the constant radius ($r = 3$) over the volume. Along the straight part of the vessel, the color representation of the tensors is green, since vessel orientation, v_3 , is through anterior-posterior direction. In the diagonal part, the color indicator becomes the mix of green and red due to diagonally oriented vectors v_3 . Tensor colors change on the edges as compared to the tensors along the centerline of the vessel, since the tensors on the edges start to become perpendicular to the tensors on the centerline, thus, the shape of the tensors become tubular along the edges of the vessel (See Figure 3.4).

3.3 Vessel tractography

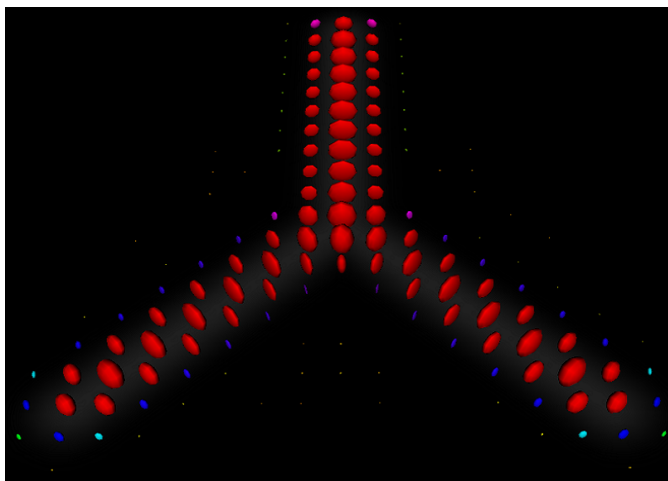
We define a vessel tractography, which traces the centerline of a vessel using the intensity based tensor \mathbf{D} , inspired by the DTI tractography that uses a diffusion tensor. Vessel tractography starts with a user defined initial seed point. The seed point is preferably selected at the center of one of the cross sections of the vessel. The tract, i.e. the 3D centerline, starts to propagate along the positive and negative directions of the eigenvector



(a) radius is 2



(b) radius is 3 (true radius)



(c) radius is 4

Figure 3.4: Estimated tensors for $60 \times 60 \times 60$ synthetic vessel volume.

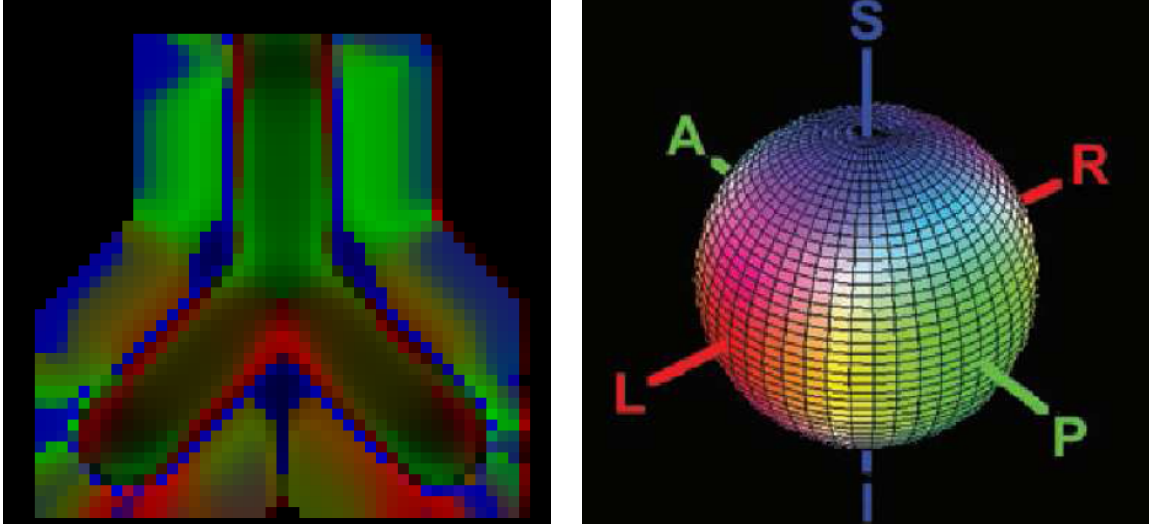


Figure 3.5: Left: Color-FA map of the estimated tensors (radius 3) for the $60 \times 60 \times 60$ synthetic vessel volume; Right: Color Hue, Red: Left-Right, Green: Anterior-Posterior, Blue: Superior-Inferior direction.

corresponding to the smallest eigenvalue of the planar tensor. For all spatial coordinates along the tract, the tensor is calculated as explained in Section 3.2. Minor vector of the tensor is obtained and a new tract coordinate $\mathbf{c}(u_n)$ is calculated by adding the \mathbf{v}_3 vector (\mathbf{v}_3 describes the principal orientation of the vessel which is the smallest eigenvector of the tensor at $\mathbf{c}(u_{n-1})$) to the current coordinate $\mathbf{c}(u_{n-1})$. To avoid tract aberrations, a streamline tractography (SLT) [74] method is preferred. SLT uses the vessel orientation by weighting it with α to compute Euler's method approximation to the parametrized tract $\mathbf{c}(u)$ as follows:

$$\mathbf{c}(u_n) = \mathbf{c}(u_{n-1}) + \alpha \frac{d\hat{\mathbf{c}}(u)}{du} \rightarrow \mathbf{c}(u_n) \approx \mathbf{c}(u_{n-1}) + \alpha \mathbf{v}_3 \quad (3.13)$$

where $\mathbf{c}(u = 0)$ is the seed point, and $0 \leq u_n \leq L$, L is the length of the vessel. The tract is computed using a piecewise linear step in the direction of \mathbf{v}_3 . Tract propagation occurs in both collinear tangent directions approximated by \mathbf{v}_3 (See Figure 3.6).

The tractography algorithm continues till pre-defined convergence criteria are satisfied:

- First convergence criterion is the mean intensity ratio between the spherical region of the seed and that of the current coordinate $\mathbf{c}(u_{n-1})$. The sphere centered at the seed

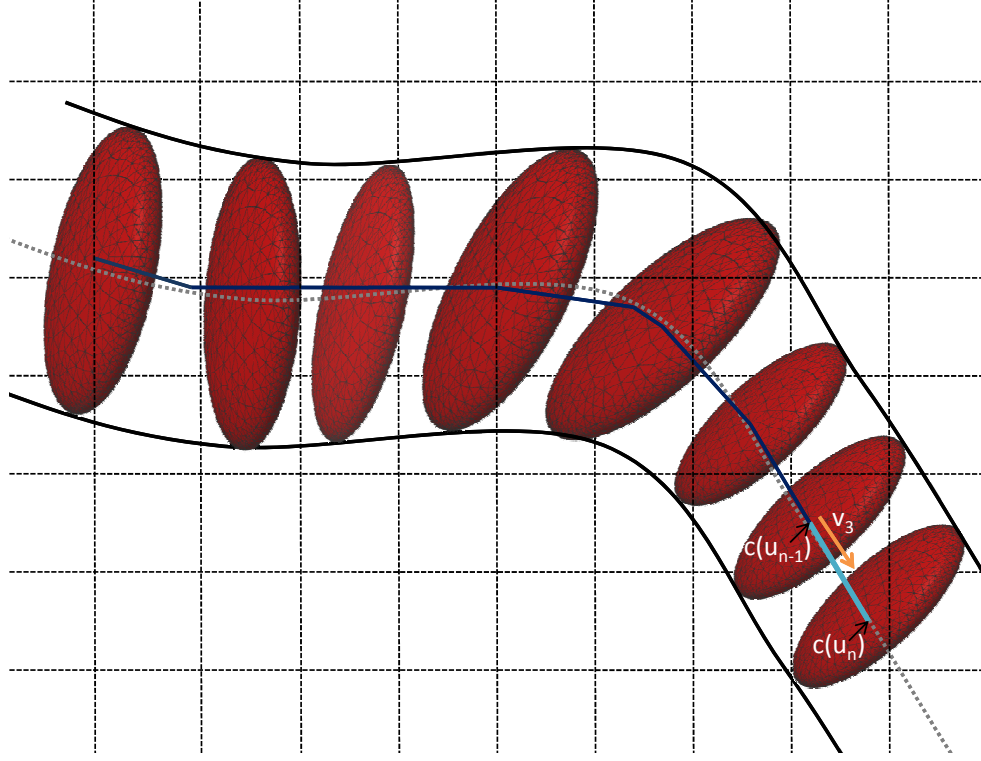


Figure 3.6: Illustration of the vessel tractography: Centerline of the vessel (black) is shown by gray. Extracted vessel tract until the current coordinate $\mathbf{c}(u_{n-1})$ is depicted by (navy blue). On the distal part of the tract (turquoise); minor vector of the planar tensor, \mathbf{v}_3 , current location, $\mathbf{c}(u_{n-1})$, and how the tract is obtained by adding the \mathbf{v}_3 direction to the current location $\mathbf{c}(u_{n-1})$ are shown.

point is defined as $sph_1 = (\mathbf{c}_{seed}, r_{seed})$ and sphere at the current coordinate $\mathbf{c}(u_{n-1})$ is $sph_2 = (\mathbf{c}(u_{n-1}), r)$, and the regions are specified as $\Omega_1 = sph_1$ and $\Omega_2 = sph_2$. If the ratio $\beta_1 = \mu_{\Omega_2}/\mu_{\Omega_1}$ is below a given threshold (I_{thresh_1}), this implies that the tract reaches the end of the vessel and the tractography stops at this point (See Figure 3.7).

- Second termination criterion is defined from the ratio $\beta_2 = \mu_{\Omega_3}/\mu_{\Omega_2}$ where $\Omega_3 = sph_3 - sph_2$ and $sph_3 = (\mathbf{c}(u_{n-1}), 2r)$. When $\mathbf{c}(u_{n-1})$ reaches the origin (coronary ostium) or the end of artery, β_2 is assumed to be approximately 1. β_2 is used both to force tract to stop at the end of vessel and to prevent the tract to diverge toward

regions around the vessel (See Figure 3.8).

- Third criterion, which stops the tract when the radius r at point $\mathbf{c}(u_{n-1})$ reaches to $r = r_{max}$, is used to avoid divergence of the vessel tract to surrounding blob regions.

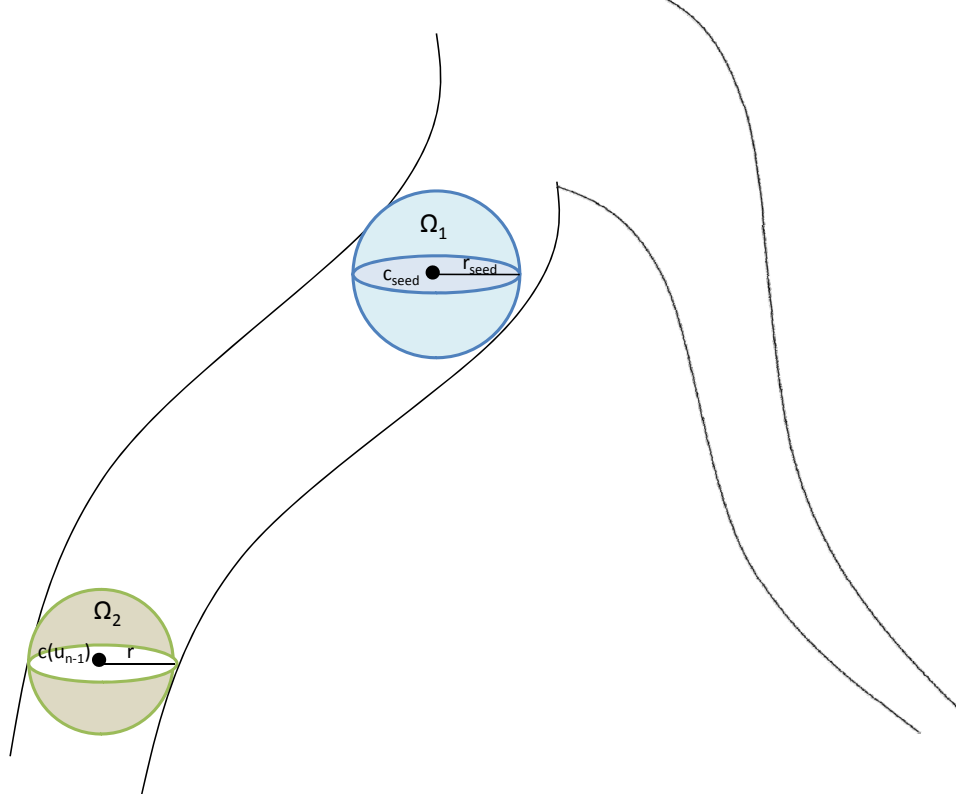


Figure 3.7: Illustration of the regions (spheres) Ω_1 and Ω_2 .

3.3.1 Centralization

Sometimes a tract or a centerline of the vessel can aberrate because of the effects of tensor perturbation. In this case, a centralization procedure should be applied to the tract. First, a multiplanar reconstruction method (MPR) (Eq. 3.14) is applied at the coordinate $\mathbf{c}(u_{n-1})$ to find a projection slice which has \mathbf{v}_3 as its normal vector. Then, \mathbf{v}_1 and \mathbf{v}_2 define the reconstructed plane. The MPR plane image is defined as

$$I_{prj}(i, j) = I(\mathbf{c}(u_{n-1}) + (i - x_c)\mathbf{v}_1 + (j - y_c)\mathbf{v}_2) \quad (3.14)$$

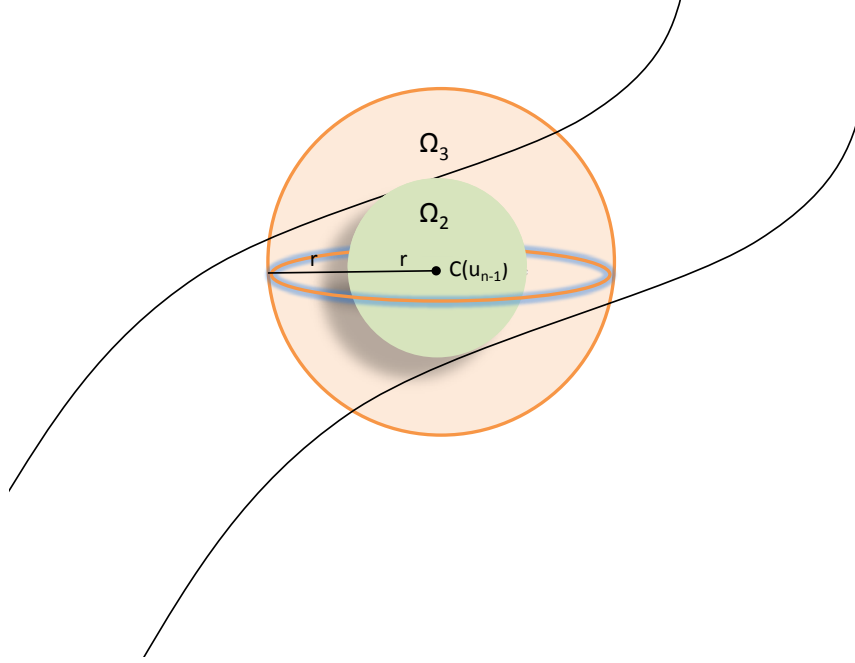


Figure 3.8: Illustration of the regions (spheres) Ω_2 and Ω_3 .

where I is the original image to be projected, I_{prj} is the projection image and x_c, y_c are the coordinate centers of the I_{prj} . After the subregion or projected plane around the coordinate through \mathbf{v}_1 and \mathbf{v}_2 is calculated, then an $r \times r$ (the radius is found during tensor fitting) kernel is applied on this plane to find the coordinate which is the center of a maximum brightness region.

This plane is chosen to be large enough to involve the vessel boundaries and surroundings near the vessel, but not very large to compromise other structures around the vessel. Typically, it is chosen as 40×40 in image coordinates. Let (x', y') represent the coordinates of the maximum brightness point, which is found in the following way:

$$(x', y') = \operatorname{argmax}_{x,y} \sum_{i,j \in N(x,y)} I_{prj}(i, j), \quad (3.15)$$

where the neighbourhood function $N(x, y)$ is expressed as:

$$N(x, y) = \{(i, j) | (x - i)^2 + (y - j)^2 \leq r^2\}. \quad (3.16)$$

Then the corresponding point in the original image is defined as

$$\mathbf{c}' = \mathbf{c}(u_{n-1}) + (x' - x_c) \frac{\mathbf{v}_1}{2} + (y' - y_c) \frac{\mathbf{v}_2}{2} \quad (3.17)$$

where \mathbf{c}' is the centralized point, which is the corrected centerline coordinate.

3.4 Branch Detection - Unsupervised Clustering

In order to extend our vessel tractography model to tubular trees, we developed a branch detection method. It is inspired from the Mohan et. al. work [10], which was based on an assumption that vessels have at most two branches to be separated. Their algorithm checks the surrounding regions around the center coordinate $\mathbf{c}(u_{n-1})$ and cluster them in a supervised way via a K-means clustering.

We propose an unsupervised clustering method, which is capable of detecting any number of branchings from a parent coordinate. In our method, we assume that the branches of the vessel tree have similar intensity distributions with the main branch. We search the branches on a spherical surface around the current coordinate in a $\frac{5}{3}\pi$ field of view, which avoids the branch candidates that are already processed (See Figure 3.9). Branch candidate coordinates are calculated as:

$$\mathbf{c}(i) = \mathbf{c}(u_{n-1}) + 2r\mathbf{g}_i, \quad \mathbf{g}_i \in \mathbf{g} \quad (3.18)$$

where \mathbf{g} represents orientations on \mathbb{S}^2 as defined in Section 3.2.

The intensity mean of the sphere, μ_{sph_1} , centered at the potential branch coordinate, $\mathbf{c}(i)$, is defined with a sphere $sph_1 = sph(\mathbf{c}(i), r)$, and the intensity mean of the sphere, μ_{sph_2} , centered at the seed, \mathbf{c}_{seed} is expressed with $sph_1 = (\mathbf{c}_{seed}, r_{seed})$. Intensity mean ratio, I_{thresh} , is applied for the potential branch candidates using $\mu_{sph_1} I_{thresh} \geq \mu_{sph_2}$. When the potential branch candidate has a mean intensity lower than $\mu_{sph_1} I_{thresh}$, the tensor fitting is applied at that coordinate. Direction of the vectors are used as a cluster classifier in our method. If \mathbf{v}_3 of the tensor of the potential branch coordinate is not in the direction of the current path, \mathbf{v}_3 and its coordinate is put into a new cluster or to an already existing cluster as follows:

- (i) When the vector \mathbf{v}_3 is closer to the directions in one of the previously formed clusters, it is inserted into an appropriate cluster with its corresponding coordinate;
- (ii) When the vector \mathbf{v}_3 has a distinct orientation, a new cluster is constructed, and this vector is added with its corresponding coordinate to that cluster.

Detected branch coordinates and orientation vectors are stacked into clusters in a $2r$ voxel distance away from the first coordinate that detected branches, c_{first} (See Figure 3.9). Then, coordinate mean of each cluster is calculated and labelled as a branch coordinate. The proposed branch detection algorithm is summarized in Algorithm 1. The algorithm is based on the assumption that the vessel displays greater intensity than structures surrounding the vessel that have a size similar to that of a vessel. We perform branch detection step each time the current point $\mathbf{c}(u_{n-1})$ moves significantly, i.e. when there is 1 voxel difference between its last location where a branch check was performed.

Algorithm 1 Branch Detection algorithm - Unsupervised Clustering Method

- 1: **Input:** Sample N directions $g_i, \forall i \in (1, N)$ uniformly off the sphere \mathbb{S}^2 , current coordinate $\mathbf{c}(u_{n-1})$, μ_{seed} intensity mean of the sphere centered at c_{seed} with radius r_{seed} , mean threshold I_{thresh} , angle thresholds $A_{thresh_1}, A_{thresh_2}$ and Cl_C (clusters of branch coordinates), Cl_V (clusters of orientation vectors). The clusters are cleared at the beginning of each tractography.
 - 2: **Output:** Updated Cl_C, Cl_V .
 - 3: Threshold the $\mathbf{g}_i^T \mathbf{v}_3 < \cos(A_{thresh_1})$ with angle threshold A_{thresh_1} to avoid searching the branches in the previously processed voxels.
 - 4: Find a branch candidate $\mathbf{c}(i)$ using Eq. 3.18.
 - 5: Eliminate the candidate coordinate $\mathbf{c}(i)$, if it is labelled as processed (the coordinates already processed are labelled by a spherical mask with the estimated r).
 - 6: Apply the tensor fitting as explained in Section 3.2; find $r(i)$ (radius), $\mathbf{v}(i)$ (vessel direction) and $\mu(i)$ (mean of the sphere with radius $r(i)$ centered at $\mathbf{c}(i)$) of the tensor for $\mathbf{c}(i)$.
 - 7: Eliminate the candidate coordinate $\mathbf{c}(i)$ for:
 - 8: **a)** \mathbf{v}_i that has overlap with the parent vector \mathbf{v}_3 ;
 - 9: **b)** $r = r_{max}$;
 - 10: **c)** $\mu(i) < \mu_{seed} I_{thresh}$
-

11: **if** Cl_C or Cl_V is empty **then**
12: Create a new cluster in Cl_V and insert $\mathbf{v}(i)$ to that cluster.
13: Create a new cluster in Cl_C and insert $\mathbf{c}(i)$ to that cluster.
14: **else**
15: Search for all vectors in each Cl_V .
16: **if** \mathbf{v}_i has a similar orientation with the vectors in each Cl_V (A_{thresh_2} is chosen as angle criteria) **then**
17: Insert \mathbf{v}_i to an appropriate cluster in Cl_V .
18: Insert \mathbf{c}_i to an appropriate cluster in Cl_C .
19: **else**
20: Create a new cluster for \mathbf{v}_i and \mathbf{c}_i ; insert them to Cl_V and Cl_C .
21: **end if**
22: **end if**

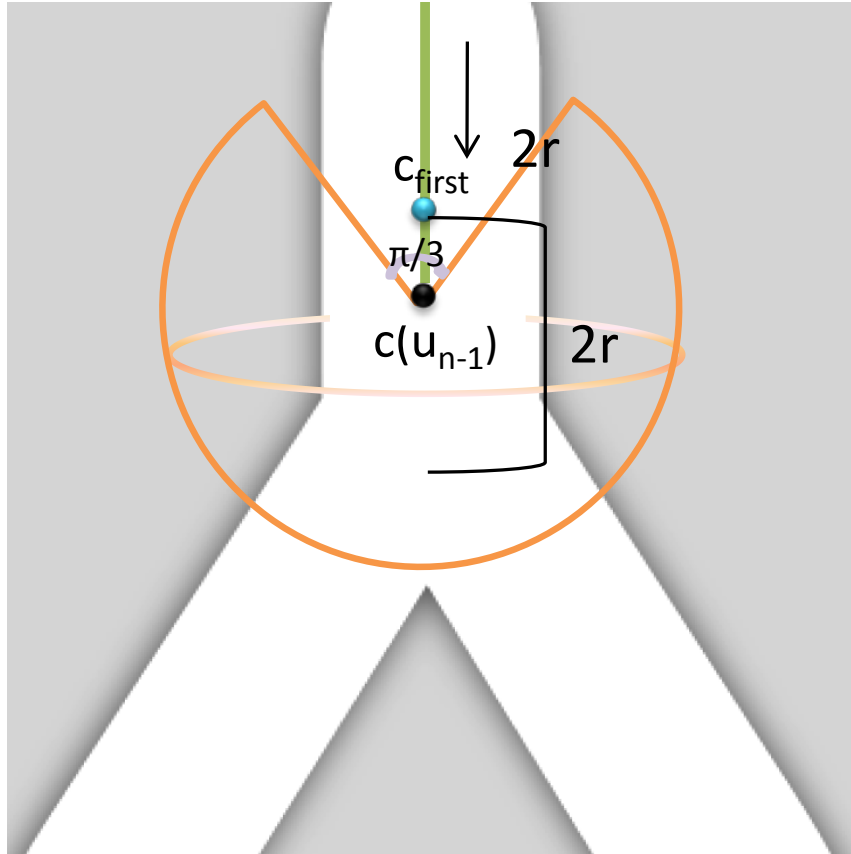


Figure 3.9: Illustration of branch detection algorithm, where the tractography direction is shown by black arrow, the estimated path until the current coordinate is depicted by green, $\frac{5}{3}\pi$ sphere cut with radius $2r$ centered at $c(u_{n-1})$ is illustrated by orange, the coordinate that first detects one or more branches is shown by a blue sphere, and referred to as c_{first} . In addition, $2r$ voxel distance for stacking of detected branches from c_{first} is shown in the sketch.

Chapter 4

Experimental Results

In this section, we first give a quantitative validation of the performance of our method on 3 synthetic vascular image volumes, and 8 CTA Rotterdam coronary segmentation challenge [77, 11] volumes with known ground truth. Next, we evaluate our method qualitatively and apply it to extract the coronary arteries from 10 CTA volumes. For each case, a single seed point is selected from each tree, then entire vessel tree is segmented automatically.

The parameters of the algorithm are fixed over all experiments as follows:

- $t_{myo} = 950$ and $t_{myo} = 1700$ are used in preprocessing step for calcium level thresholding;
- 24 unit directions on \mathbb{S}^2 are used for tensor fitting;
- 128 unit directions on \mathbb{S}^2 are used for branch detection;
- The radius range is selected between 0.25 and 4 mm in tensor fitting;
- Maximum intensity projection plane dimensions are selected as 40×40 ;
- The angle threshold, A_{thresh_1} , is chosen as $\frac{5\pi}{3}$;
- The angle threshold, A_{thresh_2} , is chosen as $\frac{\pi}{9}$;
- Algorithm's termination ratios β_1 and β_2 are chosen as 0.25 and 0.85;
- I_{thresh} , ratio of intensity mean of the spheres in branch detection is set to 0.85.

To decrease the run-time of our program, the radius range 0.25 and 4 mm is applied for the seed coordinate. By finding the radius r at the end of tensor fitting, radius range is selected between $r - 3$ and $r + 3$, which prevents to check unnecessary radius for further coordinates in tensor fitting. Moreover, radius dependency results in a smoother path, since the radius range gets narrower in tensor fitting, and the radius becomes more dependent on the radius of the previous coordinate.

The proposed vessel tractography algorithm is fully implemented in C++ environment, using Qt [78] and VTK [79] libraries for visualization.

4.1 Quantitative Validation

For the synthetic validation, the datasets are obtained from the work of Hamarneh and Jassi’s [80], which simulate volumetric images of vascular trees and generate the corresponding ground truth segmentations. We used 4 different quantitative measures for the synthetic validation as TP (True Positive), FN (False Negative), FP (False Positive) and OM (Overlap Measure) between the estimated vessel map and the ground truth vessel map, which are defined as follows:

$$TP = \frac{N_B \cap N_R}{N_R} \quad (4.1)$$

$$FN = \frac{N_R - N_B \cap N_R}{N_R} \quad (4.2)$$

$$FP = \frac{N_B - N_B \cap N_R}{N_R} \quad (4.3)$$

$$OM = 2 \frac{N_B \cap N_R}{N_B + N_R} \quad (4.4)$$

where N_R is the number of reference ground truth voxels, and N_B is the number of voxels detected by our algorithm in synthetic data. OM means overlap metric, which is a Dice similarity coefficient that approaches a value of 1.0 for results that are very similar and is near 0.0 when they share no similarly classified voxels.

Table 4.1 shows TP, FN, FP and OM rates for the three synthetic vascular datasets. We obtained high TP and OM ratios between 93% and 96%.

Figures 4.1, 4.2, 4.3 depict Hamarneh and Jassi’s [80] three synthetic vascular dataset, and the results of our algorithm on the dataset. Each top frame shows the 3D model and

Table 4.1: Segmentation results of our method on synthetic vascular images

Rate (%)	Data 1	Data 2	Data 3
TP	94.30	94.77	96.13
FN	5.7	5.23	3.87
FP	8.45	4.88	4.76
OM	93.03	93.76	95.70

sample cross-sections of the reference dataset. The user selects a single seed, which is shown with a yellow sphere, from one of the branches. Then, the entire tree is extracted automatically by our method. The branch coordinates that are found during the execution of our algorithm are shown on the left figure by red spheres. Extracted centerlines of the datasets are shown by green. Vessel trees with radial thickness are shown by pink on the right.

Recently, attempts at evaluating and comparing the performance of various algorithms for coronary artery centreline extraction from a common CTA data set have been proposed in the Rotterdam Coronary Artery Algorithm Evaluation Framework [77, 11]. As part of the 2008 MICCAI workshop 3D Segmentation in the Clinic: A Grand Challenge II”, a coronary artery tracking competition has been started. Due to lack of ground-truth segmentation, it is essential to generate a reference standard from multiple manually annotated datasets, which is an exhaustive task for the experts. One of the contributions of the works of [77, 11] is the design of a reference standard for vessel tracking data with multiple observers using the weighted averaging of 3D open curves, which in the end has become a standardized evaluation methodology for the quantitative evaluation of coronary artery centreline extraction algorithms [11]. The works involved in the coronary segmentation challenge are summarized in [11].

The major contributions of this work are defining measures for the evaluation of coronary artery centreline extraction algorithms as illustrated in Figure 4.4. There are 32 datasets presented in this framework, where 24 of data are for testing, and 8 of them are for training and the corresponding reference standard centerlines for the training data are

made publicly available. Four vessels are selected for annotation, where the first three vessels are always the right coronary artery (RCA), left anterior descending artery (LAD), and left circumflex artery (LCX). The fourth vessel is selected from the large side branches of these main coronary arteries. 37.5% of the datasets have good quality of images, 37.5% are moderate, and 25% are poor of quality. Additionally, all datasets consist of a level of calcium presence. According to the amount of interaction, methods are classified into three categories: fully automatic, semi-automatic or interactive. Most algorithm attempts on this challenge [11] are interactive methods, which need more than one seed per vessel.

Accuracy and overlap scores for the segmented vessels are calculated as described in [11]. There are three overlap scores: *Overlap* (OV), *Overlap until first error* (OF) and *Overlap with > 1.5 mm vessel* (OT). These scores measure the overlap between the segmented centerlines and a ground truth centerline derived from manual segmentations by human experts. Mathematically, overlap measures are defined as follows:

$$OV = \frac{\|TPM_{ov}\| + \|TPR_{ov}\|}{\|TPM_{ov}\| + \|TPR_{ov}\| + \|FN_{ov}\| + \|FP_{ov}\|}, \quad (4.5)$$

$$OF = \frac{\|TPR_{of}\|}{\|TPR_{of}\| + \|FN_{of}\|}, \quad (4.6)$$

$$OT = \frac{\|TPM_{ot}\| + \|TPR_{ot}\|}{\|TPM_{ot}\| + \|TPR_{ot}\| + \|FN_{ot}\| + \|FP_{ot}\|}. \quad (4.7)$$

A point on the centerline to be evaluated is marked as true positive TPR_{ov} if the distance to at least one of the connected points on the evaluated centerline is less than the annotated radius and false negative FN_{ov} otherwise. A point is marked as true positive TPM_{ov} if there is at least one connected point on the reference standard at a distance less than the radius defined at that reference point, and it is marked as false positive FP_{ov} otherwise. TPM_{of} is the number of true positive points on the reference before the first error. The first error is defined as the first FN_{ov} point when traversing from the start of the reference standard to its end, while ignoring false negative points in the first 5 mm of the reference standard, since sometimes it is hard to define the beginning of artery, and it is not of critical importance. TPM_{ot} and TPR_{ot} denote the number of true positive points until the diameter of 1.5 mm, which is assumed to be clinically relevant. FN_{ot} and FP_{ot} denote

the number of false negative and false positive points respectively. $\|\cdot\|$ represents the cardinality of set of points.

The scores are scaled so that 0 indicates complete failure, 50 corresponds to a result within the human inter-observer variability, and 100 is a perfect result. The overlap scores for our algorithm, and for each of the 8 training datasets are presented in Table 4.2. Nearly complete segmentation of the target vessels, more than 97% are on average segmented. This leads to high overlap scores, with an average of 76 for the OV score, i.e., significantly better than the human inter-observer variability.

The accuracy scores evaluate the distance to the ground truth centerline. The scores are: *Average distance* (AD), *Average distance inside vessel* (AI) and *Average distance to the clinical relevant part of a vessel* (AT). The distances and the scores are shown in Table 4.3. The average distance to the ground truth centerline is 0.44 mm, and we obtained 31.2 for average AD score. A summary of all scores are presented in Table 4.4. Comparison of our algorithm, VET (Vessel Tractography), with the top 8 methods (for further information about the methods, see [81]) in Rotterdam challenge are shown in Table 4.5. Our algorithm ranks the **5th** among **18** methods using only the training data for all. For further official evaluation, the results on Rotterdam test datasets will be submitted to the organizers of the evaluation framework.

In general, we used one seed per vessel tree, for the very low resolution and narrowing cases, we applied more seeds. In average, we used 3-4 seed per dataset. Thus, we need much less user interaction than other methods as shown in the last column of Table 4.5.

Our method is fast, since it is a centerline-based method. The runtime of our algorithm with 3D visualization is ~ 9 minutes for a complete CTA vessel tree from a volume of typical size with $512 \times 512 \times 441$ voxels. We also added an option to our vessel tractography program for single branch extraction (without branch detection), which takes between ~ 1 -2 minutes. See the Table 4.5 for the runtime comparison with other methods. Figures 4.5, 4.6, and 4.7 show visualizations for the results of training dataset 1, 2 and 6 from Rotterdam coronary artery database.

Table 4.2: Average overlap per dataset

Dataset nr.	OV		OF		OT	
	%	score	%	score	%	score
0	96.7	69.5	80.2	67.9	96.7	60.9
1	97.9	59.87	90.5	45.9	97.9	48.9
2	98.6	84.0	95.6	74.5	98.5	74.3
3	91.6	81.6	72.2	63.0	91.8	78.9
4	96.2	72.3	67.6	45.6	99.4	74.7
5	98.8	80.7	58.5	52.1	98.8	71.0
6	99.8	85.9	99.2	74.5	99.9	85.5
7	97.1	74.4	66.1	58.8	97.1	73.6
Avg.	97.1	76.0	78.7	60.3	97.5	71.0

4.2 Qualitative Validation

Next, we used our method to extract the coronary arteries from CTA volumes of 10 patients from Yeditepe University Hospital. The results are shown on Table 4.6. For a qualitative evaluation; the cardiologist expert in our project team¹ gave scores (0-5) to RCA (Right Coronary Artery), LM (Left Main), LAD (Left Anterior Descending) and LCX (Left Circumflex Artery) by considering the length, thickness and centerline of each artery.

We obtained high qualitative scores for each dataset. Extracted arteries for CTA datasets for all 10 patients are depicted in Figures 4.8 and 4.9. Our model finds the thickness for each coordinate along the centerline, thus, we can find the exact location of narrowings. Therefore, our method is capable of finding the stenosis along the arteries. According to the cardiologist expert’s view, possible abnormal narrowings along the arteries in Figures 4.8, 4.9 can be because of stenosis. Blue arrows in the images of Patient 4, 5, 6, 7 and 9 indicate the sample narrowings.

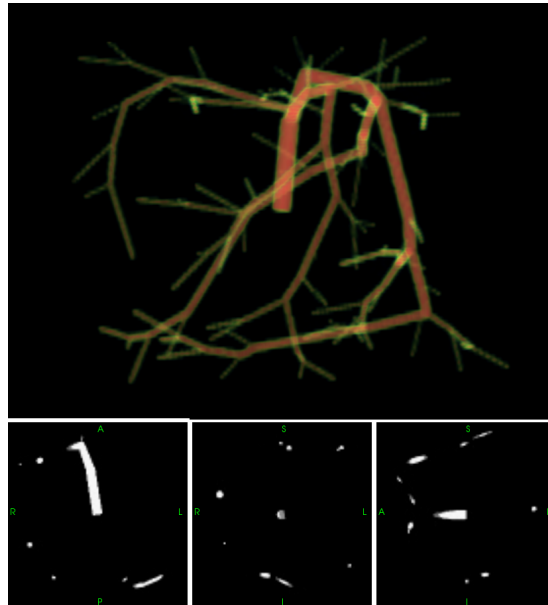
¹Prof. Dr. Muzaffer Degertekin, Cardiology Dept., Yeditepe University Hospital, Istanbul.

Table 4.3: Average accuracy per dataset

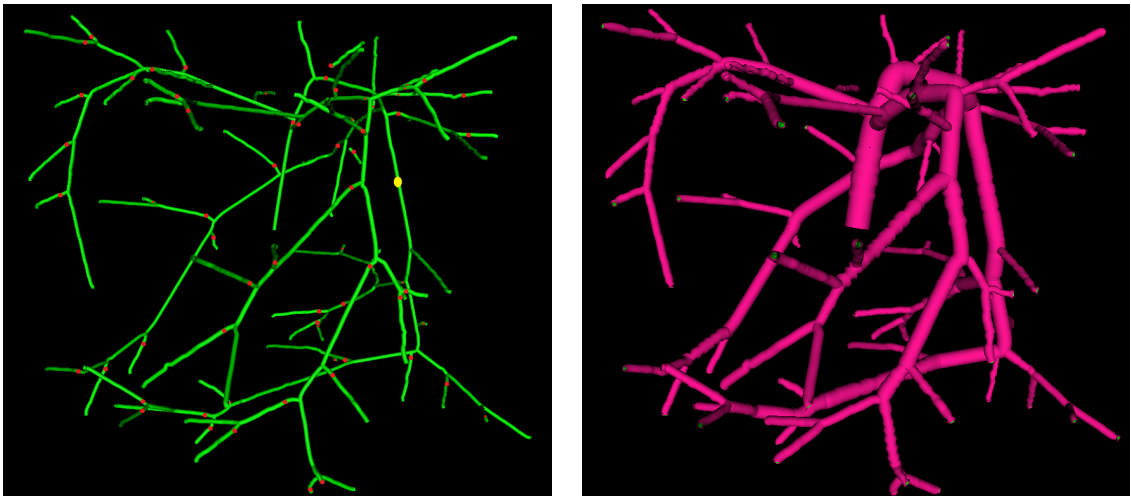
Dataset nr.	AD		AI		AT	
	mm	score	mm	score	mm	score
0	0.48	32.4	0.44	33.2	0.48	24.9
1	0.52	31.7	0.37	32.5	0.52	31.7
2	0.39	26.9	0.36	27.1	0.39	26.8
3	0.64	31.2	0.40	33.3	0.61	31.3
4	0.33	29.3	0.31	29.9	0.31	29.9
5	0.43	36.4	0.40	36.8	0.43	36.4
6	0.34	24.7	0.34	24.7	0.34	24.6
7	0.34	37.0	0.31	38.0	0.35	35.3
Avg.	0.44	31.2	0.37	32.0	0.43	30.1

Table 4.4: Summary

Measure	% / mm			score		
	min.	max.	avg.	min.	max.	avg.
OV	69.7%	100.0%	97.1%	38.8	100.0	76.0
OF	9.9%	100.0%	78.7%	4.91	100.0	60.3
OT	70.6%	100.0%	97.5%	35.3	100.0	71.0
AD	0.26mm	1.31mm	0.43mm	22.3	46.7	31.2
AI	0.22mm	0.49mm	0.37mm	22.3	49.1	31.9
AT	0.26mm	1.19mm	0.43mm	6.28	46.7	30.1

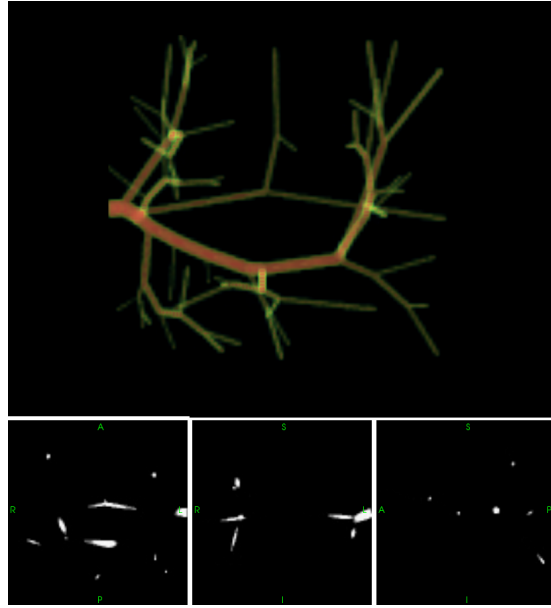


(a) Synthetic vascular dataset1; Top: Volume rendering; Bottom: slices from 3 orthogonal views.

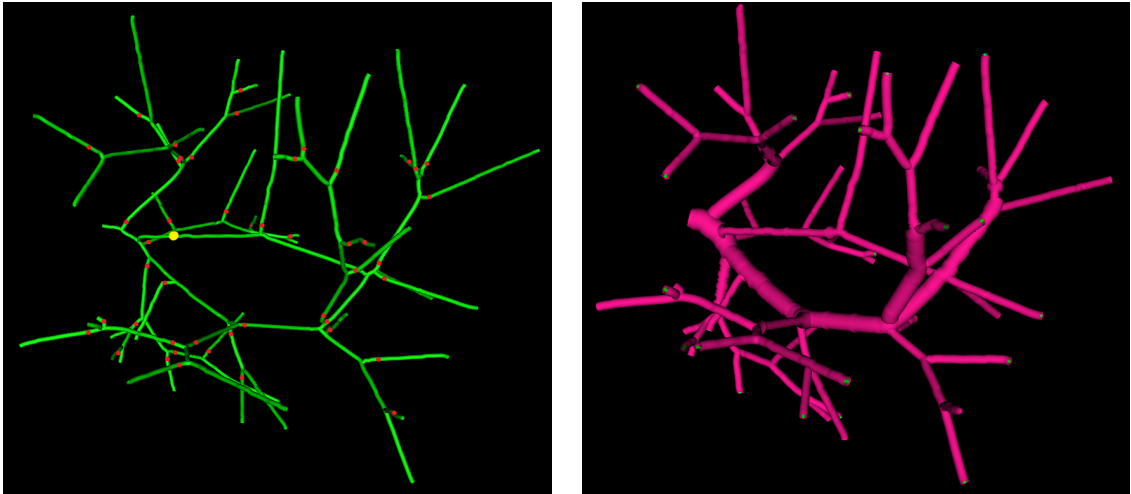


(b) Extracted centerline is indicated by green, detected branch coordinates by red, and seed point which provides the radius information of the vessel at each centerline point. (c) Extracted surface (pink) surrounds centerline,

Figure 4.1: Extracted vessel tree from the $101 \times 101 \times 101$ synthetic vascular dataset1.



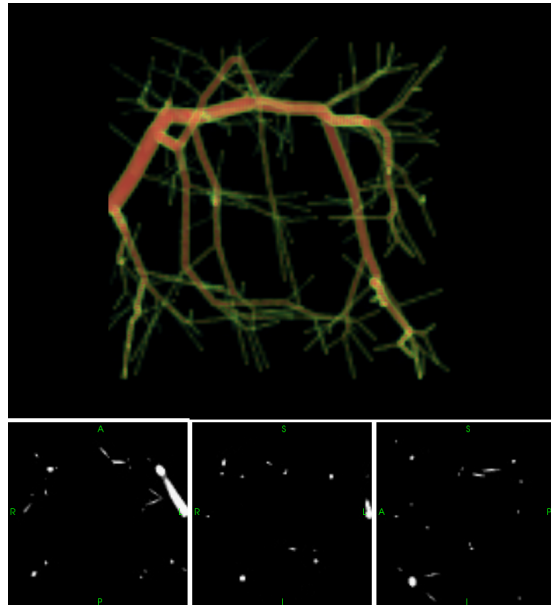
(a) Synthetic vascular dataset2; Top: Volume rendering; Bottom: slices from 3 orthogonal views.



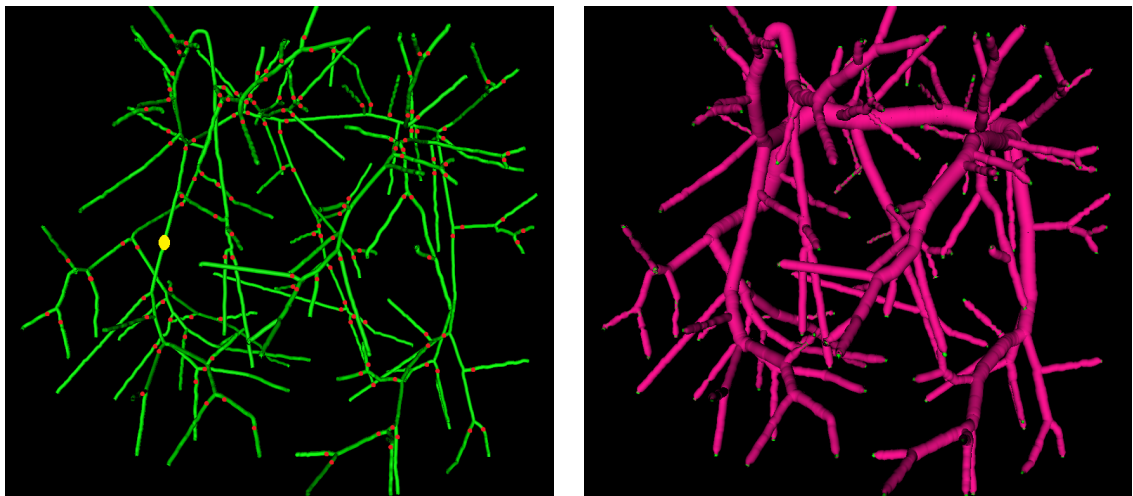
(b) Extracted centerline is indicated by green, detected branch coordinates by red, and seed point by yellow;

(c) Extracted surface (pink) surrounds centerline, which provides the radius information of the vessel at each centerline point.

Figure 4.2: Extracted vessel tree from the $101 \times 101 \times 101$ synthetic vascular dataset2.



(a) Synthetic vascular dataset3; Top: Volume rendering; Bottom: slices from 3 orthogonal views.



(b) Extracted centerline is indicated by green, detected branch coordinates by red, and seed point by yellow;

(c) Extracted surface (pink) surrounds centerline, which provides the radius information of the vessel at each centerline point.

Figure 4.3: Extracted vessel tree from the $101 \times 101 \times 101$ synthetic vascular dataset3.

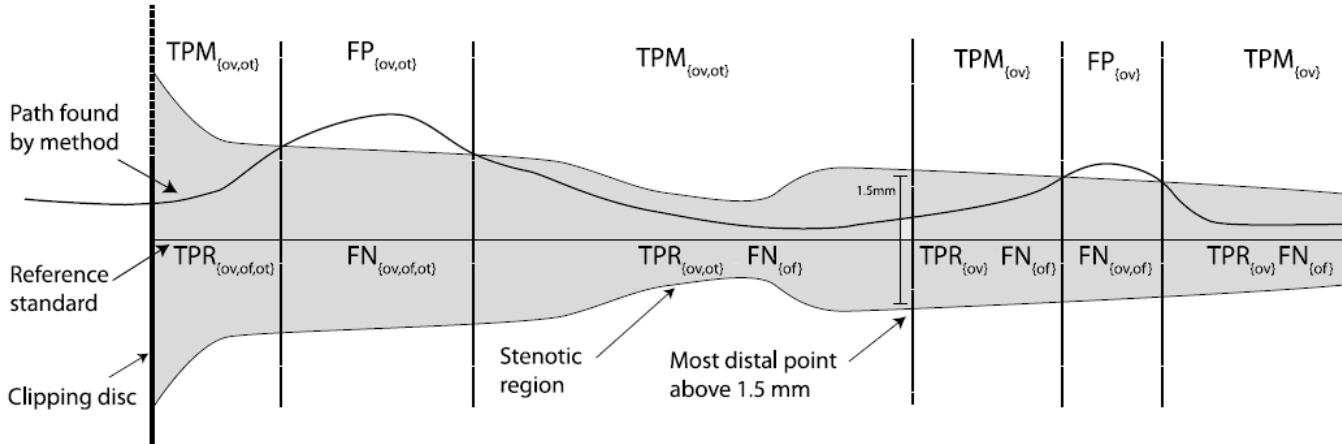
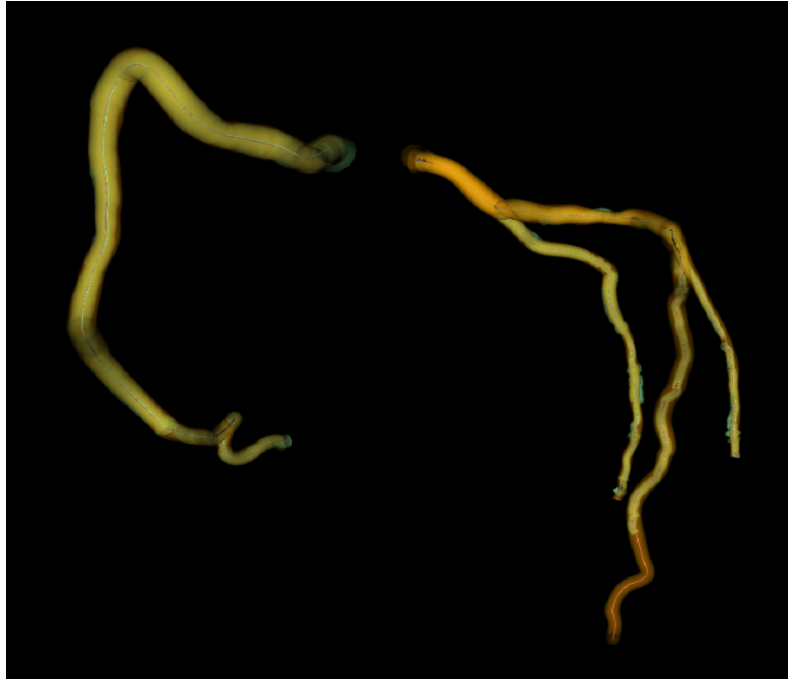


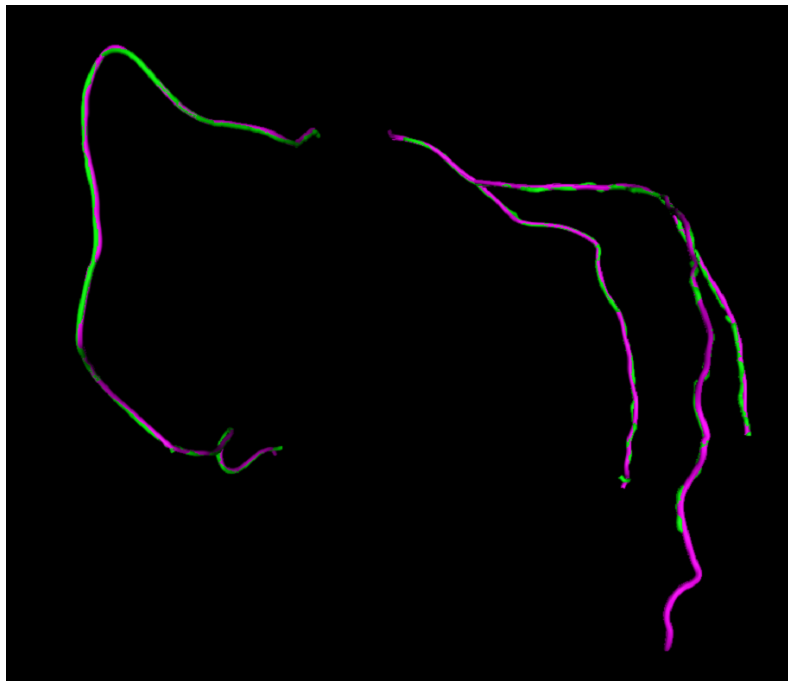
Figure 4.4: Illustration of different quantities for the analysis of vessel segmentation, adopted from [11]. The reference standard is illustrated as the horizontal line in the middle with annotated radius depicted as the grey region. The metrics used to evaluate the segmented coronary path are labelled above and below the reference standard. For further details on the metrics, see [11]

Table 4.5: Comparison of top 8 methods with our method, VET, participated in Rotterdam challenge

Method	AI		OF		OT		OV		Run time (per dataset)	User interaction (per vessel)
	mm	score	%	score	%	score	%	score		
MHT	0.24	47.9	94.6	83.2	99.5	90.0	99.3	91.6	6 min.	2 - 5
SR	0.25	49.6	73.4	64.6	96.0	81.8	95.5	77.7	22 min.	2.2
TR	0.28	43.8	68	52.9	92.8	68.3	92.2	68.4	30 min.	3
BMP	0.31	37.7	86.1	77.2	97.7	83.0	97.6	82.3	4 min.	2 (S, E)
VET	0.37	31.9	78.7	60.3	97.5	71.0	97.1	76.0	8 - 10 min.	3 - 4 (per data)
CRA	0.26	46.3	76.1	54.2	88.2	60.7	86.8	55.0	4 - 6 min.	
VC	0.32	40.0	69.7	56.8	94.4	70.3	93.7	64.4	5 min.	
DFMF	0.31	40.5	78.3	60.3	93.0	67.3	89.2	52.2	4 - 8 min.	
KBMP	0.41	30.4	92.7	85.3	98.1	89.4	98.1	88.1	7 hrs	1 (E)

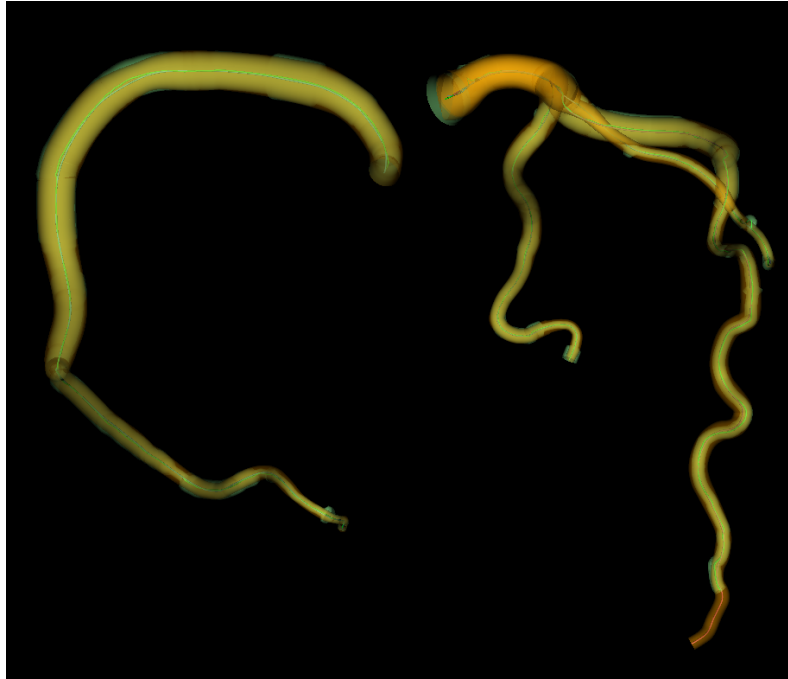


(a) Visualization of the ground truth (orange) and corresponding vessel trees (pale green) segmented by proposed framework.



(b) Visualization of centerline of the ground truth (purple) and corresponding vessel trees (green) segmented by proposed framework.

Figure 4.5: Visualization of the result from experiments for quantitative validation using the Rotterdam cardiac data set # 1.

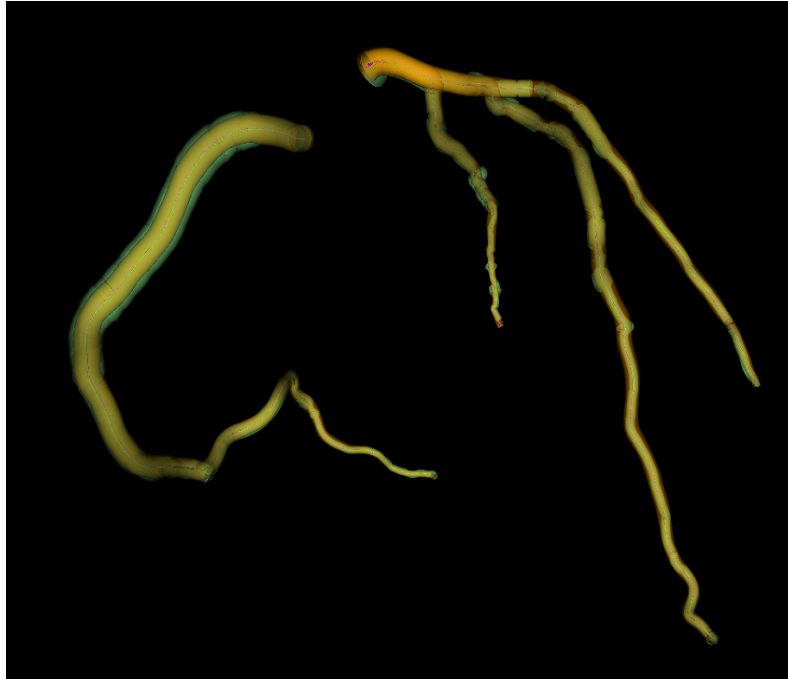


(a) Visualization of the ground truth (orange) and corresponding vessel trees (pale green) segmented by proposed framework.

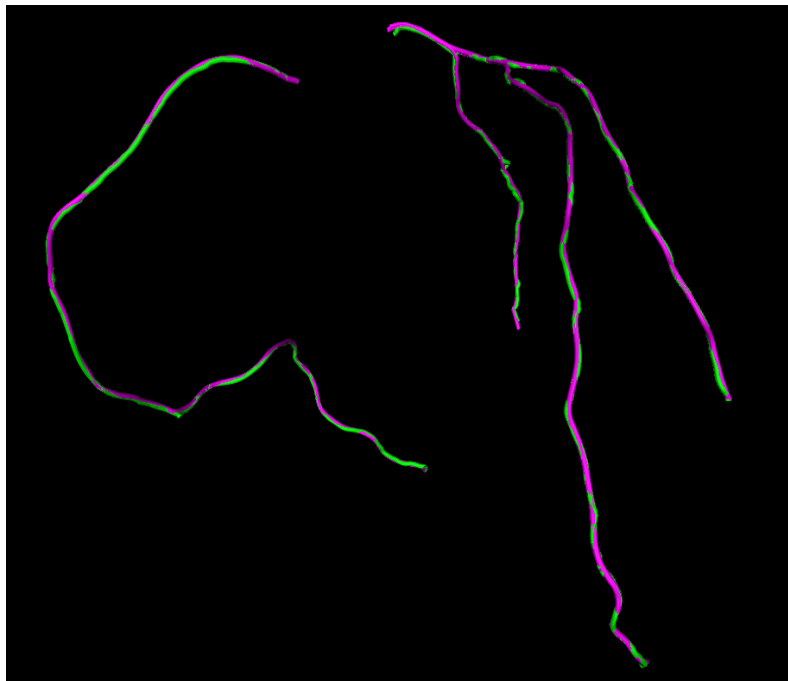


(b) Visualization of centerline of the ground truth (purple) and corresponding vessel trees (green) segmented by proposed framework.

Figure 4.6: Visualization of results from experiments for quantitative validation using the Rotterdam cardiac data set # 2.



(a) Visualization of the ground truth (orange) and corresponding vessel trees (pale green) segmented by proposed framework.

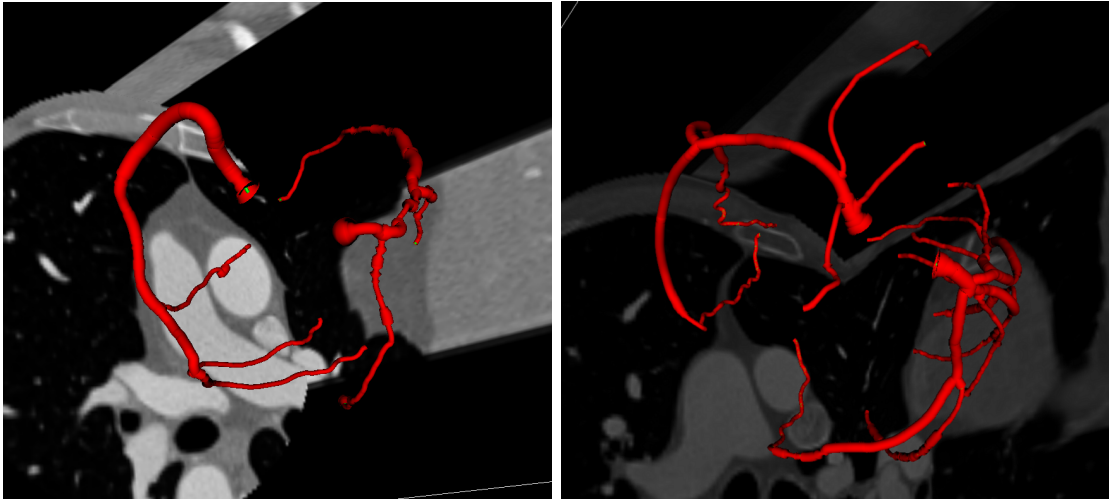


(b) Visualization of centerline of the ground truth (purple) and corresponding vessel trees (green) segmented by proposed framework.

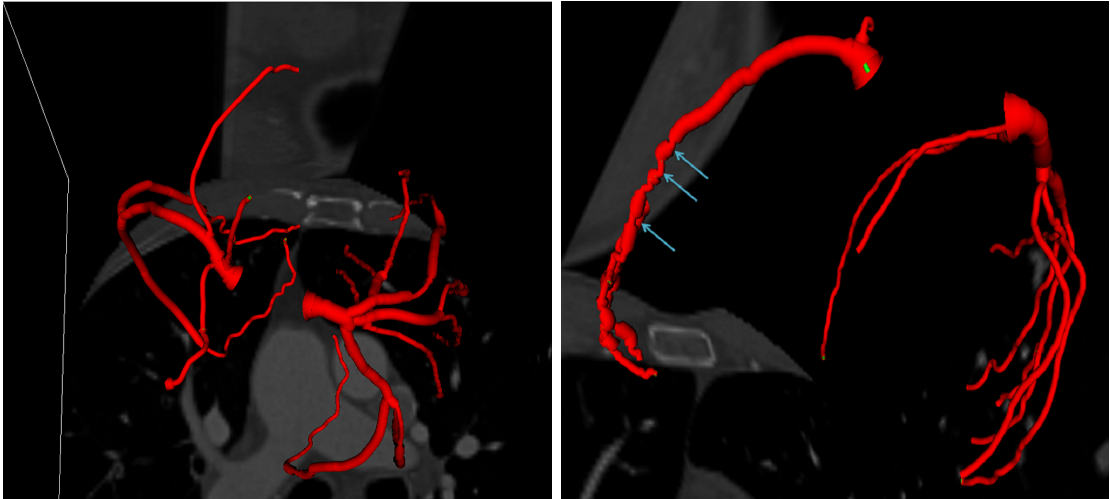
Figure 4.7: Visualization of results from experiments for quantitative validation using the Rotterdam cardiac data set # 6.

Table 4.6: Visual scores of our method on 10 CTA datasets from Pt 1 to Pt 10

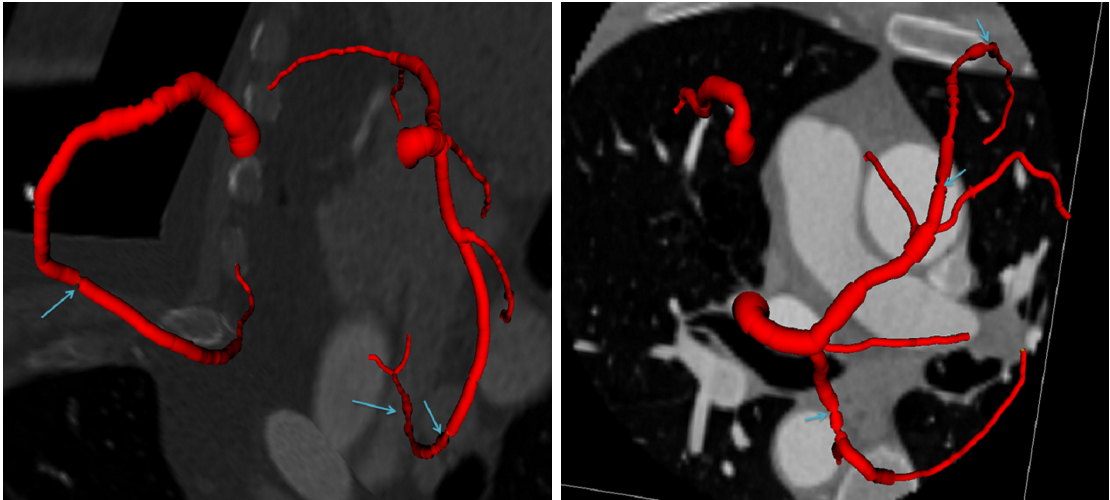
	Pt 1	Pt 2	Pt 3	Pt 4	Pt 5	Pt 6	Pt 7	Pt 8	Pt 9	Pt 10
RCA	5	5	5	5	5	5	5	4	5	5
LM	5	5	5	5	5	5	5	5	4.5	5
LAD	5	5	5	5	4.5	4.5	5	4	4.5	5
LCX	4	5	5	5	5	4.5	5	4	5	5



(a) Left: patient 1, Right: patient 2

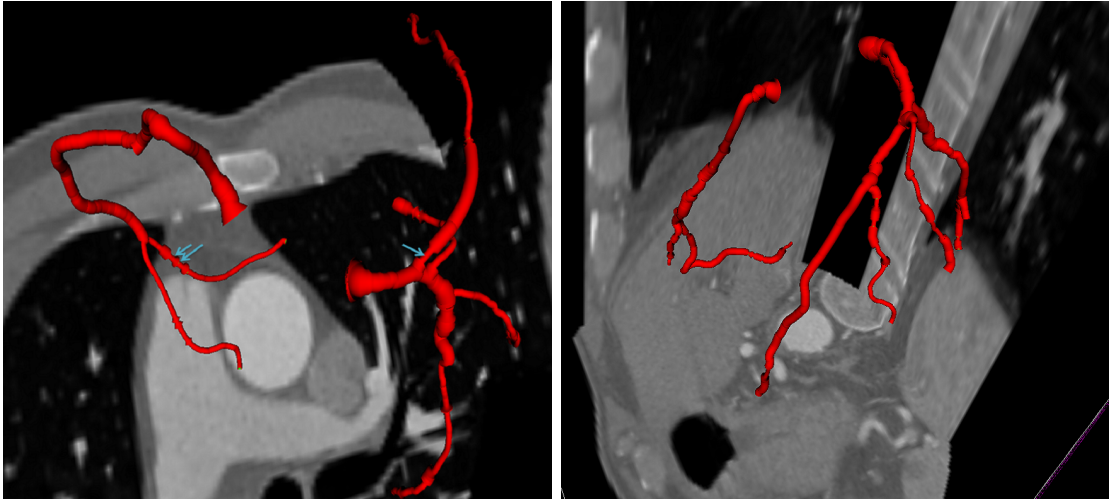


(b) Left: patient 3, Right: patient 4



(c) Left: patient 5, Right: patient 6

Figure 4.8: Visualization of extracted arteries from CTA volumes of patient # 1 to 6.



(a) Left: patient 7, Right: patient 8



(b) Left: patient 9, Right: patient 10

Figure 4.9: Visualization of extracted arteries from CTA volumes of patient # 7 to 10.

Chapter 5

Conclusions and Future Work

In this thesis, we presented a model for extraction of coronary arteries from Computed Tomography Angiography (CTA) scans, and created a visual model of arteries, which may be used as a virtual medical navigation tool to detect possible anomalies on arteries. For this purpose, we designed a fast and novel tubular structure segmentation method, which constructs an intensity-based tensor that traces a vessel, and used it in a tractography framework, inspired from DTI field.

In this direction, we introduced our tensor based segmentation method, where we brought a DTI tractography approach to centerline extraction of the tubular structures by constructing an intensity based tensor model. We described computations of the vessel orientation, centerline (central lumen line) and its thickness at the same time. We demonstrated how an entire coronary tree can be captured by the proposed automatic branch detection algorithm.

For the experiments and validations, we first quantitatively validated our algorithm on three complex synthetic vascular datasets, where we obtained high overlap ratios $94.2\% \pm 1.9$. We also quantitatively evaluated our method on the training datasets of Rotterdam Coronary Artery database [81], which provides a framework where several algorithms can be compared with the others, and obtained also high overlap ratio as 97% in average. In the qualitative experiments of our work, a cardiologist expert gave scores(0-5) to LM (Left Main), LAD (Left Anterior Descending), LCX (Left Circumflex), and RCA (Right Coronary Artery) coronary arteries in 10 CTA datasets according to the length, thickness and centerline of each artery. We obtained high scores for each dataset. Ad-

ditionally, as our method finds the thickness for each coordinate along the centerline, we were able to visualize the vessel surface, and show any abnormalities, such as stenosis, along the arteries.

Future directions of our work include:

- Single tensor models are not sufficient in junctions, a multiple-tensor model [82] can be created to handle the junction problems (See the sketch in Figure 5.1);
- New potential measurement can be proposed to represent possible vessel intensity distributions;
- New vessel models, i.e instead of cylinder, can be proposed e.g cone, half ellipsoid;
- High-contrasted MRA of peripheral vessels would also be a potential application of this method.

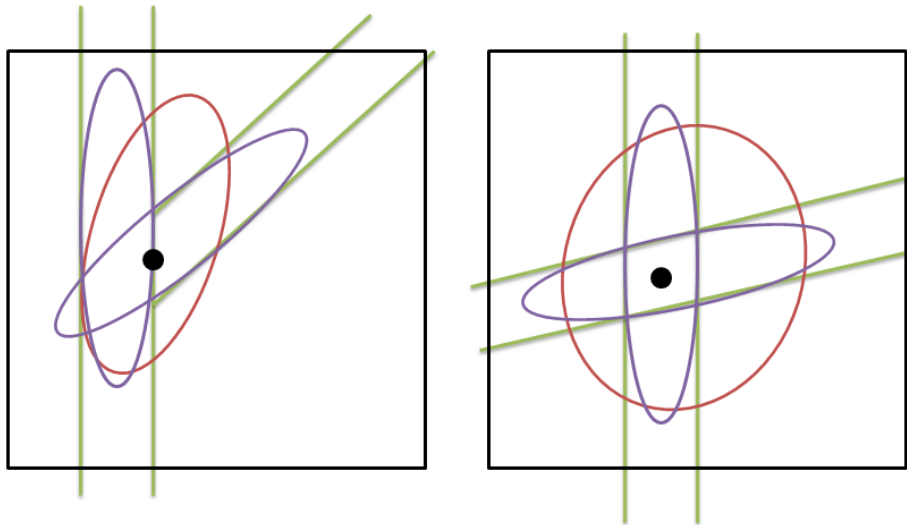


Figure 5.1: Sample sketches for the junction problem. Edges of the vessels are shown with green color. Black circle depicts the junction coordinate. Red ellipsoid indicates the single tensor fitting at the junction coordinate, where single tensor is insufficient for the representation of the junction. Purple ellipsoids illustrates the result of multiple-tensor fitting.

Bibliography

- [1] WHO, “The 10 leading causes of death by broad income group (2004),” *World Health Organization Media Center, editor.*, October 2008.
- [2] I.-K. Jang, B. E. Bouma, D. H. Kang, S. J. Park, S. W. Park, K. B. Seung, K. B. Choi, M. Shishkov, K. Schlendorf, E. Pomerantsev, S. L. Houser, H. T. Aretz, and G. J. Tearney, “Visualization of coronary atherosclerotic plaques in patients using optical coherence tomography: comparison with intravascular ultrasound.” *Journal of the American College of Cardiology*, vol. 39, no. 4, pp. 604–609, Feb. 2002.
- [3] S. Clare, “Functional mri : Methods and applications,” *PhD Thesis, University of Nottingham*, 1997.
- [4] R. Manniesing, M. Viergever, and W. Niessen, “Vessel enhancing diffusionA scale space representation of vessel structures,” *Medical Image Analysis*, vol. 10, no. 6, pp. 815–825, Dec. 2006.
- [5] H. Li and A. J. Yezzi, “Vessels as 4-d curves: Global minimal 4-d paths to extract 3-d tubular surfaces and centerlines,” *IEEE Trans. Med. Imaging*, vol. 26, no. 9, pp. 1213–1223, 2007.
- [6] Y. Yang, “Image segmentation and shape analysis of blood vessels with applications to coronary atherosclerosis,” *PhD Thesis, Georgia Institute of Technology*, 2007.
- [7] D. Nain, A. J. Yezzi, and G. Turk, “Vessel segmentation using a shape driven flow,” in *MICCAI (1)*, 2004, pp. 51–59.

- [8] S. Worz and K. Rohr, "Segmentation and quantification of human vessels using a 3-d cylindrical intensity model," *Image Processing, IEEE Transactions on*, vol. 16, no. 8, pp. 1994–2004, aug. 2007.
- [9] J. Tyrrell, E. di Tomaso, D. Fuja, R. Tong, K. Kozak, R. Jain, and B. Roysam, "Robust 3-d modeling of vasculature imagery using superellipsoids," *Medical Imaging, IEEE Transactions on*, vol. 26, no. 2, pp. 223–237, feb. 2007.
- [10] C. Westbrook, *MRI at a glance*, 2nd ed. Wiley-Blackwell, 2010.
- [11] M. Schaap, C. T. Metz, T. van Walsum, A. G. van der Giessen, A. C. Weustink, N. R. Mollet, C. Bauer, H. Bogunovice, C. Castro, X. Deng, E. Dikici, T. O'Donnell, M. Frenay, O. Friman, M. H. Hoyos, P. H. Kitslaar, K. Krissian, C. Kühnel, M. A. Luengo-Oroz, and M. Orkisz, "Standardized evaluation methodology and reference database for evaluating coronary artery centerline extraction algorithms," *Medical Image Analysis*, vol. 13, pp. 701–714, 2009.
- [12] A. F. Frangi, W. J. Niessen, K. L. Vincken, and M. A. Viergever, "Multiscale Vessel Enhancement Filtering," *Medical Image Computing and Computer-Assisted Intervention MICCAI'98*, pp. 130–137, 1998.
- [13] E. N. Marieb and K. Hoehn, *Human Anatomy And Physiology*, 7th ed. Benjamin-Cummings Publishing Company, May 2006.
- [14] P. Libby, "Inflammation in atherosclerosis," *Nature*, vol. 420, pp. 868–874, 2002.
- [15] Z. A. Fayad and V. Fuster, "Clinical Imaging of the High-Risk or Vulnerable Atherosclerotic Plaque," *Circ Res*, vol. 89, no. 4, pp. 305–316, Aug. 2001.
- [16] Z. A. Fayad, V. Fuster, K. Nikolaou, and C. Becker, "Concepts coronary angiography and plaque imaging: Current and potential future computed tomography and magnetic resonance imaging for noninvasive," 2010.
- [17] S. Cetin, G. Unal, A. Demir, and M. Degertekin, "Vessel tractography using an intensity based tensor model," *The MICCAI Workshop on Computing and Visualization for (Intra)Vascular Imaging (CVII)*, 2011.

- [18] D. L. Pham, C. Xu, and J. L. Prince, “A Survey of Current Methods in Medical Image Segmentation,” in *Annual Review of Biomedical Engineering*, 2000, vol. 2, pp. 315–338.
- [19] Z. Ma, J. M. R. S. Tavares, and R. M. N. Jorge, “A review on the current segmentation algorithms for medical images.” in *IMAGAPP*, A. Ranchordas and J. Tavares, Eds. INSTICC Press, 2009, pp. 135–140.
- [20] Z. Ma, J. a. M. Tavares, R. N. Jorge, and T. Mascarenhas, “A review of algorithms for medical image segmentation and their applications to the female pelvic cavity,” *Computer Methods in Biomechanics and Biomedical Engineering*, vol. 13, no. 2, pp. 235–246, 2010.
- [21] I. N. Bankman, Ed., *Handbook of Medical Image Processing and Analysis*, 2nd ed. Academic Press, Dec. 2008.
- [22] T. Yoo, Ed., *Insight Into Images 'Principles and Practice for Segmentation, Registration and Image Analysis'*. A K Peters Ltd., 2004.
- [23] S. Aylward and E. Bullitt, “Initialization, noise, singularities, and scale in height ridge traversal for tubular object centerline extraction,” *Medical Imaging, IEEE Transactions on*, vol. 21, no. 2, pp. 61 –75, feb. 2002.
- [24] C. Bauer and H. Bischof, “Extracting curve skeletons from gray value images for virtual endoscopy,” in *Proceedings of the 4th international workshop on Medical Imaging and Augmented Reality*, ser. MIAR '08. Berlin, Heidelberg: Springer-Verlag, 2008, pp. 393–402.
- [25] C. Florin, N. Paragios, and J. Williams, “Particle filters, a quasi-monte carlo solution for segmentation of coronaries,” in *Medical Image Computing and Computer-Assisted Intervention*, 2005, pp. 246–253.
- [26] T. Koller, G. Gerig, G. Szekely, and D. Dettwiler, “Multiscale detection of curvilinear structures in 2-d and 3-d image data,” in *Computer Vision, 1995. Proceedings., Fifth International Conference on*, jun 1995, pp. 864 –869.

- [27] C. Lorenz, I. Carlsen, T. Buzug, C. Fassnacht, and J. Weese, “Multi-scale line segmentation with automatic estimation of width, contrast and tangential direction in 2D and 3D medical images,” in *CVRMed-MRCAS’97*, ser. Lecture Notes in Computer Science, J. Troccaz, E. Grimson, and R. Mösges, Eds. Berlin/Heidelberg: Springer Berlin / Heidelberg, 1997, vol. 1205, ch. 24, pp. 233–242.
- [28] Y. Sato, S. Nakajima, H. Atsumi, T. Koller, G. Gerig, S. Yoshida, and R. Kikinis, “3D Multi-scale line filter for segmentation and visualization of curvilinear structures in medical images,” in *CVRMed-MRCAS ’97: Proceedings of the First Joint Conference on Computer Vision, Virtual Reality and Robotics in Medicine and Medial Robotics and Computer-Assisted Surgery*. London, UK: Springer-Verlag, 1997, pp. 213–222.
- [29] S. D. Olabbarriaga, W. J. Niessen, and M. Breeuwer, “Evaluation of hessian-based filters to enhance the axis of coronary arteries in ct images,” in *Computer Assisted Radiology and Surgery*, 2003, pp. 1191–1196.
- [30] P. Orłowski and M. Orkisz, “Efficient computation of Hessian-based enhancement filters for tubular structures in 3D images,” *IRBM*, vol. 30, no. 3, pp. 128–132, Jun. 2009.
- [31] G. Sapiro, “Geometric partial differential equations in image analysis: past, present, and future,” *Image Processing, International Conference on*, vol. 3, pp. 3001–4 vol.3, Aug. 1995.
- [32] J. Weickert, “A review of nonlinear diffusion filtering,” in *Proceedings of the First International Conference on Scale-Space Theory in Computer Vision*, ser. SCALE-SPACE ’97. London, UK: Springer-Verlag, 1997, pp. 3–28.
- [33] K. Krissian, “Flux-based anisotropic diffusion applied to enhancement of 3-d angiograms,” *IEEE Trans. Med. Imaging*, vol. 21, no. 11, pp. 1440–1442, 2002.
- [34] L. Risser, F. Plouraboue, and X. Descombes, “Gap Filling of 3-D Microvascular Networks by Tensor Voting,” *Medical Imaging, IEEE Transactions on*, vol. 27, no. 5, pp. 674–687, 2008.

- [35] M. W. Law and A. C. Chung, “Three dimensional curvilinear structure detection using optimally oriented flux,” in *Proceedings of the 10th European Conference on Computer Vision: Part IV*. Berlin, Heidelberg: Springer-Verlag, 2008, pp. 368–382.
- [36] D. Lesage, E. D. Angelini, I. Bloch, and G. Funka-Lea, “Design and study of flux-based features for 3d vascular tracking,” in *Proceedings of the Sixth IEEE international conference on Symposium on Biomedical Imaging: From Nano to Macro*, ser. ISBI’09. Piscataway, NJ, USA: IEEE Press, 2009, pp. 286–289.
- [37] C. Kirbas and F. Quek, “A review of vessel extraction techniques and algorithms,” *ACM Comput. Surv.*, vol. 36, pp. 81–121, June 2004.
- [38] P. Felkel, R. Wegenkittl, and A. Kanitsar, “Vessel Tracking in Peripheral CTA Datasets - An Overview,” in *IEEE Spring Conference on Computer Graphics (SCCG 2001)*, 2001, pp. 232–239.
- [39] J. S. Suri, K. C. Liu, L. Reden, and S. Laxminarayan, “A review on MR vascular image processing algorithms: Acquisition and prefiltering: part I,” *IEEE T. Inf. Technol. Biomed.*, vol. 6, no. 4, pp. 324–337, Dec. 2002.
- [40] J. S. Suri, K. Liu, L. Reden, and S. Laxminarayan, “A review on mr vascular image processing: skeleton versus nonskeleton approaches: part ii,” *IEEE Transactions on Information Technology in Biomedicine*, vol. 6, no. 4, pp. 338–350, 2002.
- [41] K. Bühler, P. Felkel, and A. L. Cruz, “Geometric methods for vessel visualization and quantification – a survey,” in *In Geometric Modelling For Scientific Visualization*. Springer-Verlag, 2002, pp. 399–420.
- [42] D. Lesage, E. D. Angelini, I. Bloch, and G. Funka-Lea, “A review of 3D vessel lumen segmentation techniques,” *Med. Imag. Anal.*, vol. 13, no. 6, pp. 819–845, Dec. 2009.
- [43] D. P. Zhang, “Coronary artery segmentation and motion modelling,” *PhD Thesis, Imperial College London*, 2010.
- [44] Y. L. Chang and X. Li, “Adaptive image region-growing,” *Image Processing, IEEE Transactions on*, vol. 3, no. 6, pp. 868–872, nov 1994.

- [45] P. Soille, *Morphological Image Analysis: Principles and Applications*, 2nd ed. Se-
caucus, NJ, USA: Springer-Verlag New York, Inc., 2003.
- [46] R. Rodríguez, T. E. Alarcón, and O. Pacheco, “A new strategy to obtain robust
markers for blood vessels segmentation by using the watersheds method,” *Comput.
Biol. Med.*, vol. 35, pp. 665–686, October 2005.
- [47] N. Passat, C. Ronse, J. Baruthio, J. P. Armspach, and J. Foucher, “Watershed and
multimodal data for brain vessel segmentation: Application to the superior sagittal
sinus,” *Image Vision Comput.*, vol. 25, pp. 512–521, April 2007.
- [48] N. Passat, C. Ronse, J. Baruthio, J. P. Armspach, and C. Maillot, “Magnetic reso-
nance angiography: From anatomical knowledge modeling to vessel segmentation,”
Medical Image Analysis, vol. 10, no. 2, pp. 259–274, Apr. 2006.
- [49] M. H. F. Wilkinson and M. A. Westenberg, “Shape preserving filament enhancement
filtering,” in *Proceedings of the 4th International Conference on Medical Image Com-
puting and Computer-Assisted Intervention*, ser. MICCAI '01. London, UK, UK:
Springer-Verlag, 2001, pp. 770–777.
- [50] B. Caldaïrou, B. Naegel, and N. Passat, “Segmentation of complex images based
on component-trees: Methodological tools,” in *Proceedings of the 9th International
Symposium on Mathematical Morphology and Its Application to Signal and Image
Processing*, ser. ISMM '09. Berlin, Heidelberg: Springer-Verlag, 2009, pp. 171–180.
- [51] B. Bouraoui, C. Ronse, J. Baruthio, N. Passat, and P. Germain, “3D segmentation
of coronary arteries based on advanced Mathematical Morphology techniques,” *Com-
puterized Medical Imaging and Graphics*, vol. 34, no. 5, pp. 377–387, July 2010.
- [52] D. S. Bloomberg and L. Vincent, “Pattern matching using the blur hit - miss trans-
form,” *Journal of Electronic Imaging*, vol. 9, pp. 140–150, 2000.
- [53] T. Deschamps and L. D. Cohen, “Fast extraction of minimal paths in 3d images and
applications to virtual endoscopy,” *Med. Imag. Anal.*, vol. 5, no. 4, pp. 281 – 299,
2001.

- [54] T. Deschamps and L. Cohen, “Fast extraction of tubular and tree 3d surfaces with front propagation methods,” in *Pattern Recognition, 2002. Proceedings. 16th International Conference on*, vol. 1, 2002, pp. 731 – 734 vol.1.
- [55] L. D. Cohen and T. Deschamps, “Segmentation of 3d tubular objects with adaptive front propagation and minimal tree extraction for 3d medical imaging.” *Comput Methods Biomech Biomed Engin*, vol. 10, no. 4, pp. 289–305, 2007.
- [56] L. Cohen and R. Kimmel, “Global minimum for active contour models: A minimal path approach,” *International Journal of Computer Vision*, vol. 24, pp. 57–78, 1997.
- [57] M. Gulsum and H. Tek, “Robust vessel tree modeling,” in *Medical Image Computing and Computer-Assisted Intervention – MICCAI 2008*, ser. Lecture Notes in Computer Science, D. Metaxas, L. Axel, G. Fichtinger, and G. Székely, Eds. Springer Berlin / Heidelberg, 2008, vol. 5241, pp. 602–611.
- [58] V. Mohan, G. Sundaramoorthi, and A. Tannenbaum, “Tubular surface segmentation for extracting anatomical structures from medical imagery,” *IEEE Trans. Med. Imag.*, pp. 1945–1958, 2010.
- [59] F. Benmansour and L. D. Cohen, “Tubular structure segmentation based on minimal path method and anisotropic enhancement,” *Int. J. Comput. Vision*, vol. 92, pp. 192–210, April 2011.
- [60] S. Osher and J. A. Sethian, “Fronts propagating with curvature-dependent speed: Algorithms based on hamilton-Jacobi formulations,” *Journal of Computational Physics*, vol. 79, pp. 12–49, 1988.
- [61] E. Angelini, Y. Jin, and A. Laine, “State of the art of level set methods in segmentation and registration of medical imaging modalities,” in *Handbook of Biomedical Image Analysis- Registration Models*, J. Suri and S. Laximinarayan, Eds. Kluwer Academic/ Plenum Publishers, 2005, pp. 47–102.

- [62] L. M. Lorigo, O. D. Faugeras, W. E. Grimson, R. Keriven, R. Kikinis, A. Nabavi, and C. F. Westin, “CURVES: curve evolution for vessel segmentation.” *Med Image Anal*, vol. 5, no. 3, pp. 195–206, 2001.
- [63] R. Manniesing, M. Viergever, and W. Niessen, “Vessel axis tracking using topology constrained surface evolution,” *Medical Imaging, IEEE Transactions on*, vol. 26, no. 3, pp. 309–316, march 2007.
- [64] X. Zhu, Z. Xue, X. Gao, Y. Zhu, and S. Wong, “Voles: Vascularity-oriented level set algorithm for pulmonary vessel segmentation in image guided intervention therapy,” in *Biomedical Imaging: From Nano to Macro, 2009. ISBI '09. IEEE International Symposium on*, 28 2009-july 1 2009, pp. 1247–1250.
- [65] O. Friman, M. Hindennach, C. Kühnel, and H.-O. Peitgen, “Multiple hypothesis template tracking of small 3D vessel structures,” *Med. Imag. Anal.*, vol. 14, no. 2, pp. 160–171, Apr. 2010.
- [66] K. Krissian, G. Malandain, N. Ayache, R. Vaillant, Y. Troussset, I. S. Antipolis, and S. A. C. (france, “Model based detection of tubular structures in 3d images,” 2000.
- [67] S. Zambal, J. Hladuvka, A. Kanitsar, and K. Buhler, “Shape and appearance models for automatic coronary artery tracking,” *In MICCAI 2008 Contest: 3D Segmentation in Clinic: A Grand Challenge*, 2008.
- [68] Y. Zhang, K. Chen, and S. T. Wong, “3d interactive centerline extraction,” *In MICCAI 2008 Contest: 3D Segmentation in Clinic: A Grand Challenge*, 2008.
- [69] L. Antiga and D. Steinman, “Robust and objective decomposition and mapping of bifurcating vessels,” *Medical Imaging, IEEE Transactions on*, vol. 23, no. 6, pp. 704–713, june 2004.
- [70] H. Li, A. Yezzi, and L. Cohen, “3d multi-branch tubular surface and centerline extraction with 4d iterative key points,” in *Proceedings of the 12th International Conference on Medical Image Computing and Computer-Assisted Intervention: Part II*, ser. MICCAI '09. Berlin, Heidelberg: Springer-Verlag, 2009, pp. 1042–1050.

- [71] E. R. Melhem, S. Mori, G. Mukundan, M. A. Kraut, M. G. Pomper, and P. C. van Zijl, “Diffusion Tensor MR Imaging of the Brain and White Matter Tractography,” *Am. J. Roentgenol.*, vol. 178, no. 1, pp. 3–16, Jan. 2002.
- [72] B. J. Jellison, A. S. Field, J. Medow, M. Lazar, M. S. Salamat, and A. L. Alexander, “Diffusion tensor imaging of cerebral white matter: A pictorial review of physics, fiber tract anatomy, and tumor imaging patterns,” *AJNR*, vol. 25, no. 3, pp. 356–369, 2004.
- [73] A. J. Taylor, “Diffusion tensor imaging: Evaluation of tractography algorithm performance using ground truth phantoms,” *PhD Thesis, Virginia Polytechnic Institute and State University*, 2004.
- [74] P. J. Basser, S. Pajevic, C. Pierpaoli, and A. Aldroubi, “Fiber tract following in the human brain using dt-mri data,” *Magn. Reson. Med*, 2002.
- [75] O. Ciccarelli, G. J. Parker, A. T. Toosy, W. C. A. Kingshott, G. J. Barker, P. A. Boulby, D. H. Miller, and A. J. Thompson, “From diffusion tractography to quantitative white matter tract measures: a reproducibility study,” *Neuroimage*, vol. 18, no. 2, pp. 348–59, 2003.
- [76] K. Krissian and G. Malandain, “Synthetical test images for vascular segmentation algorithms,” <http://lmi.bwh.harvard.edu/research/vascular/SyntheticVessels/SyntheticVesselImages.html>.
- [77] C. Metz, M. Schaap, T. van Walsum, A. van der Giessen, A. Weustink, N. Mollet, G. P. Krestin, and W. Niessen, “Editorial: 3d segmentation in the clinic: A grand challenge ii - coronary artery tracking, miccai 2008 workshop proceedings,” 2008.
- [78] Nokia, “Qt,” <http://qt.nokia.com>.
- [79] W. Schroeder, K. Martin, and B. Lorensen, “The visualization toolkit, third edition. kitware inc,” <http://www.vtk.org>.
- [80] G. Hamarneh and P. Jassi, “Vascusynth: Simulating vascular trees for generating volumetric image data with ground-truth segmentation and tree analysis,” *Computerized Medical Imaging and Graphics*, vol. 34, no. 8, pp. 605 – 616, 2010.

- [81] M. Schaap, C. Metz, T. V. Walsum, and W. Niessen, “Rotterdam coronary artery algorithm evaluation framework,” <http://coronary.bigr.nl/centerlines/>.
- [82] D. S. Tuch, “Q-ball imaging,” *Magnetic Resonance in Medicine*, vol. 52, no. 6, pp. 1358–1372, Dec. 2004.